The Astrophysical Journal, 917:9 (22pp), 2021 August 10 https://doi.org/10.3847/1538-4357/abf4c3

Discovery of a Fast Iron Low-ionization Outflow in the Early Evolution of the Nearby Tidal Disruption Event AT 2019qiz

Tiara Hung[1], Ryan J. Foley[1], S. Veilleux[2,3], S. B. Cenko[3,4], Jane L. Dai[5], Katie Auchettl[1,6,7], Thomas G. Brink[8], Georgios Dimitriadis[1], Alexei V. Filippenko[8,9], S. Gezari[2,3], Thomas W.-S. Holoien[10,13], Charles D. Kilpatrick[1], Brenna Mockler[1], Anthony L. Piro[10], Enrico Ramirez-Ruiz[1,11], César Rojas-Bravo[1], Matthew R. Siebert[1], Sjoert van Velzen[2,12], and WeiKang Zheng[8]

[1] Department of Astronomy and Astrophysics, University of California, Santa Cruz, CA 95064, USA; tiarahung@ucsc.edu
[2] Department of Astronomy, University of Maryland, College Park, MD 20742, USA
[3] Joint Space-Science Institute, University of Maryland, College Park, MD 20742, USA
[4] Astrophysics Science Division, NASA Goddard Space Flight Center, MC 661, Greenbelt, MD 20771, USA
[5] Department of Physics, University of Hong Kong, Pokfulam Road, Hong Kong, People's Republic of China
[6] School of Physics, The University of Melbourne, Parkville, VIC 3010, Australia
[7] ARC Centre of Excellence for All Sky Astrophysics in 3 Dimensions (ASTRO 3D), Australia
[8] Department of Astronomy, University of California, Berkeley, CA 94720-3411, USA
[9] Miller Institute for Basic Research in Science, University of California, Berkeley, CA 94720, USA
[10] The Observatories of the Carnegie Institution for Science, 813 Santa Barbara Street, Pasadena, CA 91101, USA
[11] DARK, Niels Bohr Institute, University of Copenhagen, Lyngbyvej 2, DK-2100 Copenhagen, Denmark
[12] Center for Cosmology and Particle Physics, New York University, NY 10003, USA
Received 2020 November 3; revised 2021 March 22; accepted 2021 April 1; published 2021 August 9

Abstract

We report the results of ultraviolet (UV) and optical photometric and spectroscopic analysis of the tidal disruption event (TDE) AT 2019qiz. Our follow-up observations started <10 days after the source began to brighten in the optical and lasted for a period of six months. Our late-time host-dominated spectrum indicates that the host galaxy likely harbors a weak active galactic nucleus. The initial Hubble Space Telescope (HST) spectrum of AT 2019qiz exhibits an iron and low-ionization broad absorption line (FeLoBAL) system that is seen for the first time in a TDE. This spectrum also bears a striking resemblance to that of Gaia16apd, a superluminous supernova. Our observations provide insights into the outflow properties in TDEs and show evidence for a connection between TDEs and engine-powered supernovae at early phases, as originally suggested by Metzger & Stone. In a time frame of 50 days, the UV spectra of AT 2019qiz started to resemble those of previous TDEs with only high-ionization broad absorption lines. The change in UV spectral signatures is accompanied by a decrease in the outflow velocity, which began at 15,000 km s^{-1} and decelerated to ∼10,000 km s^{-1}. A similar evolution in the Hα emission-line width further supports the speculation that the broad Balmer emission lines are formed in TDE outflows. In addition, we detect narrow absorption features on top of the FeLoBAL signatures in the early HST UV spectrum of AT 2019qiz. The measured H I column density corresponds to a Lyman-limit system, whereas the metal absorption lines (such as N V, C IV, Fe II, and Mg II) are likely probing the circumnuclear gas and interstellar medium in the host galaxy.

Unified Astronomy Thesaurus concepts: Black hole physics (159); High energy astrophysics (739); Galaxy accretion disks (562)

1. Introduction

Tidal disruption events (TDEs) refer to the transient phenomena where a star on a close passage to a supermassive black hole (SMBH) is torn apart under tidal stress (Hills 1975). For a star that initially traveled on a parabolic orbit, the disruption unbinds about half of the stellar mass while the bound other half assembles into an accretion disk and feeds the black hole until the debris streams are drained. In scenarios where disk formation is efficient, the onset of accretion resulting from a TDE is set by the fallback time ($t_{\rm fallback}$), which corresponds to the time it takes for the most bound debris on highly eccentric orbits to return to the pericenter (e.g., $t_{\rm fallback} = 41\ M_{\rm BH,6}^{1/2}$ days, where $M_{\rm BH,6}$ is the black hole mass in units of $10^6\ M_\odot$; Lodato et al. 2009). The gravitational potential energy liberated by the infalling gas is then converted to radiation across the electromagnetic spectrum, thus allowing a TDE to be detected by observers (Frank & Rees 1976; Rees 1988).

Observationally, X-ray, ultraviolet (UV), and optical sky surveys have identified nearly five dozen TDEs (e.g., Komossa & Bade 1999; Komossa & Greiner 1999; Esquej et al. 2007; Levan et al. 2011; Gezari et al. 2012; Holoien et al. 2016; van Velzen et al. 2020). However, these events, depending on the wavelength of discovery, exhibit a dichotomy in their properties. While the X-ray-detected TDEs are characterized by thermal emission that is consistent with the accretion model, most optically detected TDEs appear to lack or have very weak ($\lesssim 10^{-2}\ L_{\rm UV}$) X-ray emission (e.g., Holoien et al. 2019a; van Velzen et al. 2019, 2021). In particular, the optically detected events tend to have temperatures that are 1–2 orders of magnitude lower than those of their X-ray counterparts (van Velzen et al. 2011; Arcavi et al. 2014; Holoien et al. 2014; Hung et al. 2017). The optical TDEs are also able to maintain roughly the same temperature over a timescale of months.

The discrepancy between the two observational populations of TDEs may arise from the biggest uncertainty in the current TDE framework, which is whether the stellar debris can

[13] NHFP Einstein Fellow.

circularize efficiently following a TDE. Circularization requires the bound debris in highly eccentric orbits to lose a large amount of orbital energy to form a circular disk at twice the pericenter radius, $2R_p$ (conservation of specific angular momentum). In the classical scheme, the energy is dissipated efficiently via shocks produced by self-intersection at the pericenter (Rees 1988; Evans & Kochanek 1989; Phinney 1989; Ramirez-Ruiz & Rosswog 2009). This assumption is challenged by recent simulations and analytical calculations that find circularization to be extremely inefficient in certain regions of parameter space (Dai et al. 2015; Guillochon & Ramirez-Ruiz 2015; Shiokawa et al. 2015; Bonnerot et al. 2016; Hayasaki et al. 2016; Svirski et al. 2017). This possibility lays the foundation for an alternative mechanism in which the UV and optical emission in TDEs is powered by stream–stream collision shocks (Piran et al. 2015; Shiokawa et al. 2015). However, the stream–stream collision model is radiatively inefficient (Mockler & Ramirez-Ruiz 2020), which naturally leads to a slower light-curve evolution that is at odds with the observed $t^{-5/3}$ decline (theoretical mass fallback rate) in several TDEs (Metzger & Stone 2016).

In TDEs where disk formation is efficient and where radiation is driven by the inner accretion flows, a reprocessing layer at 10–100 R_T (where R_T is the tidal radius) is often invoked to explain the lower temperature in optical TDEs. Some studies suggest that the bound debris could build up a hydrostatic envelope around the SMBH to reprocess the X-ray and extreme ultraviolet (EUV) radiation released by accretion (Loeb & Ulmer 1997; Guillochon & Ramirez-Ruiz 2013), while others suggest that outflows could be the major reprocessing material in TDEs (Miller 2015; Metzger & Stone 2016; Piro & Lu 2020). Indeed, radiation-driven winds are a natural consequence of TDEs given that a "super-Eddington" phase should be common among stellar disruptions by black holes of mass $M_{\rm BH} \lesssim 10^7\ M_\odot$ (Strubbe & Quataert 2009; Wu et al. 2018). For previous TDEs, the observed temperatures and luminosities generally correspond to an ejecta mass that is greater than 1 $M_\odot$ (Matsumoto & Piran 2021).

Multiwavelength follow-up observations of TDEs have detected winds across a wide range of velocities. X-ray observations of ASASSN-14li revealed highly ionized outflows moving at both low and high velocities, from a few hundred km s^{-1} to 0.2c (Miller et al. 2015; Kara et al. 2018). The UV spectrum of ASASSN-14li also shows signs of a low-velocity outflow (Cenko et al. 2016), which has a velocity similar to that of the slower X-ray gas found by Miller et al. (2015). In the same event, radio observations are also supportive of the presence of either a subrelativistic outflow (Alexander et al. 2016) or an off-axis relativistic jet (van Velzen et al. 2016). Including AT 2019qiz, the subject of this paper, blueshifted broad absorption lines (BALs) that correspond to outflow velocities of 5000–15,000 km s^{-1} are detected in four out of five TDEs that have Hubble Space Telescope (HST) UV follow-up spectroscopy, with the exception of ASASSN-14li (Brown et al. 2018; Blagorodnova et al. 2019; Hung et al. 2019). Orientation effects may explain why BALs are absent from some TDEs (Parkinson et al. 2020).

Contrary to the late-time observational properties of TDEs, which tend to be more uniform as the reprocessing layer becomes transparent and allows one to probe the accretion disk directly (van Velzen et al. 2019; Jonker et al. 2020), early-time observations are expected to exhibit a higher degree of diversity in the flare properties. Early-time multiwavelength observations of TDEs are critical for understanding debris-stream evolution and super-Eddington accretion in TDEs, though they have rarely been obtained. To date, there are only a handful of TDEs with published pre-peak multiband light curves (e.g., ASASSN-18pg and ASASSN-19bt; Holoien et al. 2019b, 2020). Among these, ASASSN-19bt has the most densely sampled rising optical light curve because it is located in the TESS Continuous Viewing Zone.

AT 2019qiz is the most well-observed TDE since ASASSN-19bt, with a wealth of early-time multiwavelength data. Here we present the analysis of the UV and optical data of AT 2019qiz, the current record holder for the nearest TDE, at redshift $z = 0.0151$. We note that Nicholl et al. (2020, hereafter N20) also analyzed the evolution of UV and optical broadband photometry and optical spectroscopy of AT 2019qiz. However, our analysis has a stronger focus on the unique multiepoch HST UV spectra that have not been reported before. In addition, our *ugri* light curves were obtained independently at a higher cadence than that of N20 at early times.

This paper is structured as follows. The observations, including photometry and spectroscopy at UV and optical wavelengths, are discussed in Section 2. We present the procedures and results of our analysis in Section 3. Specifically, in Section 3.3 we detail the evolution and the identification of broad and narrow UV absorption lines in the HST spectra. We discuss in Section 4 the implications of our results and the origin of the UV absorption lines. Section 5 presents our conclusions.

2. Observations and Data Reduction

AT 2019qiz is a fast-evolving nuclear transient in the nearby galaxy ($z = 0.0151$) 2MASX J04463790–1013349. It was first discovered by the ATLAS (Tonry et al. 2018) on 2019 September 18 (UT dates are used throughout this paper) in the orange filter and subsequently by the Zwicky Transient Facility (ZTF; Bellm et al. 2019) on 2019 September 19 in the r filter; thus, it goes by the multiple names ATLAS19vfr and ZTF19abzrhgq. The most recent preflare nondetection was provided by ZTF on 2019 September 16 with an upper limit of $g > 19.22$ mag. We classified AT 2019qiz as a TDE from a Keck I Low-Resolution Imaging Spectrometer (LRIS; Oke et al. 1995) spectrum obtained on 2019 September 25 (Siebert et al. 2019) while still on the rise. Given the proximity of the TDE and the early classification, multiwavelength follow-up observations were triggered by the science community. Notably, AT 2019qiz was reported to be detected at radio frequencies and rising in 2019 October and November (ATel #13334; O'Brien et al. 2019).

We detail the follow-up observations that are analyzed in this paper in the subsections below. Throughout the paper, we adopt a flat ΛCDM cosmology with $H_0 = 67.4$ km s^{-1} Mpc^{-1} and $\Omega_m = 0.315$ as measured by the Planck mission (Planck Collaboration et al. 2020). The time difference (Δt) is expressed in rest-frame time with respect to the peak of the g-band light curve at MJD 58763.93. All of the magnitudes are expressed in the AB system (Oke & Gunn 1983).

AT 2019qiz was simultaneously monitored by the Ultraviolet Optical Telescope (UVOT; Gehrels et al. 2004; Roming et al. 2005) and the X-ray Telescope (XRT) on board the Neil Gehrels Swift Observatory (Gehrels et al. 2004) during its flaring state. The X-ray emission from AT 2019qiz peaks at $\sim 10^{41}$ erg s^{-1} in the 0.3–10 keV band, which is 2–3 orders of magnitude weaker than the UV and optical emission (N20).

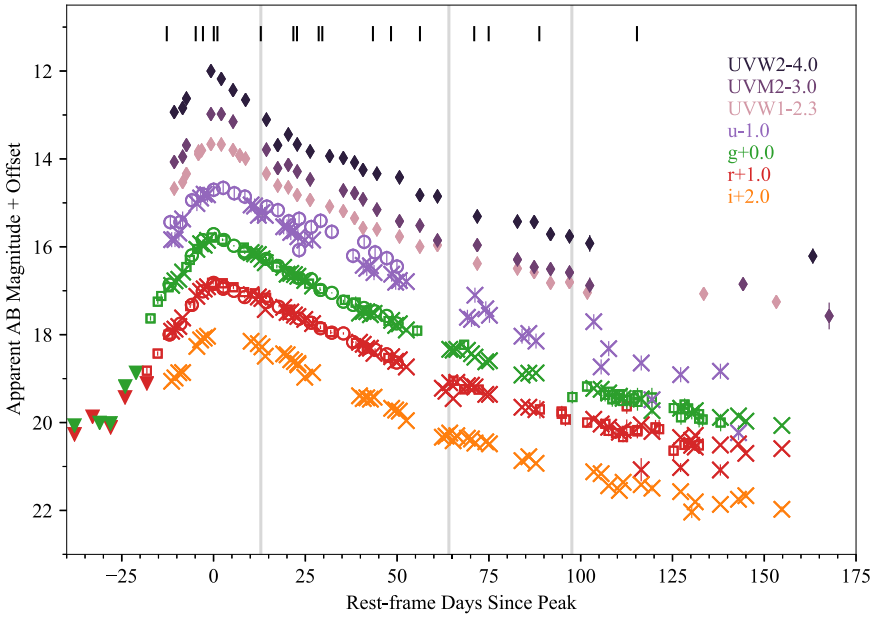

Figure 1. Multiwavelength light curves of AT 2019qiz in AB magnitudes. Photometry obtained with Swift, ZTF, LCO, and Swope is marked with diamonds, squares, circles, and crosses, respectively. The triangles indicate the upper limits in the *g* and *r* filters. The light curves are color-coded by filters and offset by a constant to aid visualization. The host-galaxy contribution has been removed from all the photometry points obtained with ground-based optical telescopes. Although we did not subtract host-galaxy light from the Swift UV filters, the contamination is negligible compared to the transient light. We indicate the HST epochs with gray vertical lines, whereas the short black vertical lines mark the epochs with optical spectroscopic observations.

Given that the Swift XRT data set has already been analyzed by N20 and is independent of our other analysis, we reference their reported luminosity and hardness ratio where appropriate without repeating the data reduction and analysis in this work.

All data for AT 2019qiz have been corrected for Milky Way foreground extinction assuming an extinction curve according to Cardelli et al. (1989) with $R_V = 3.1$ and $E(B-V) = 0.0939 \pm 0.0088$ mag (Schlafly & Finkbeiner 2011).

2.1. HST STIS Spectra

We obtained three epochs of UV spectra of AT 2019qiz with the HST Space Telescope Imaging Spectrograph (STIS) (GO-16026; PI Hung) on 2019 October 21, December 12, and 2020 January 15. The spectra were obtained through a $52'' \times 0\farcs2$ aperture. For the near-UV (NUV) and far-UV (FUV) MAMA detectors, the G140L and G230L gratings were used to cover the spectral ranges 1150–1730 Å and 1570–3180 Å at resolutions of 1.2 Å and 2.2 Å, respectively. During the first two visits, the observation was obtained over a single HST orbit, with three equal exposures of 170 s in the NUV and three equal exposures of 335 s in the FUV. The observations obtained in the last visit consist of three 692 s exposures in the NUV and three 876 s exposures in the FUV, totaling two HST orbits. We used an inverse-variance weighting method to combine the one-dimensional (1D) spectra at the same epoch that were output by the HST pipeline.

2.2. Optical Photometry

Following the classification of AT 2019qiz as a TDE on $\Delta t = -13$ days, we triggered photometric and spectroscopic monitoring spanning about six months (between 2019 September and 2020 March) before the TDE became too faint and Sun-constrained. Figure 1 shows the light curves of AT 2019qiz observed by the Swift UVOT and ground-based optical facilities including Las Cumbres Observatory (LCO), ZTF, and the Swope telescope at the Las Campanas Observatory. We list the photometric data in Table A1. Data reduction with each instrument is detailed in the following subsections.

2.2.1. ZTF Photometry

AT 2019qiz was simultaneously observed in the ZTF Mid-Scale Innovations Program field in both *g* and *r* with a cadence of 3 days. The ZTF real-time pipeline performs standard image reduction and subtraction with respect to ZTF template images and distributes the events as alert packets on each observing night (Bellm et al. 2019; Masci et al. 2019). We accessed the public alerts of AT 2019qiz via LCO MARS[14] and used the magnitude of the template-subtracted point-spread function to generate the light curves. The last ZTF detection was obtained on 2020 February 25 in *g* as ZTF stopped monitoring the field containing AT 2019qiz. We measured a signal-to-noise-ratio (S/N) weighted offset of $0\farcs13 \pm 0\farcs17$ from the ZTF *g* and *r* data, confirming that the transient is coincident with the galaxy nucleus, as expected for a TDE.

2.2.2. Swope Photometry

Optical photometry of AT 2019qiz in *ugri* was obtained with the 1 m Swope telescope from 2019 September 26 to 2020 March 1 with a cadence of 2–5 days. The images were reduced using the `photpipe` imaging and photometry pipeline (Rest et al. 2005, 2014). We subtracted the bias and flattened each frame using bias and sky-flat images obtained on the same night and in the same instrumental configuration as each AT 2019qiz image. The images were registered and geometric distortion was removed using Two Micron All Sky Survey (2MASS) astrometric standards (Cutri et al. 2003). Using `hotpants` (Becker 2015), we subtracted pre-discovery

[14] https://Mars.lco.global

Table 1
Observation Details of the Optical Spectra of AT 2019qiz

Obs. Date	Phase (days)	Telescope + Instrument	Slit Width	Grism/Grating	Exp. Time (s)
2019-09-25	−13	Keck + LRIS	1.″0	600/400+400/8500	450 (blue), 438 (red)
2019-10-03	−5	Shane + Kast	2.″0	452/3306+300/7500	3660 (blue), 3600 (red)
2019-10-05	−3	Shane + Kast	2.″0	452/3306+300/7500	930 (blue), 2 × 450 (red)
2019-10-08	0	Shane + Kast	2.″0	452/3306+300/7500	1560 (blue), 1500 (red)
2019-10-09	1	SOAR + Goodman	1.″0	400 m2	720
2019-10-21	13	SOAR + Goodman	1.″0	400 m2	2 × 720
2019-10-30	22	Shane + Kast	2.″0	452/3306+300/7500	1230 (blue), 2 × 600 (red)
2019-10-31	23	Shane + Kast	2.″0	452/3306+300/7500	1560 (blue), 1500 (red)
2019-11-06	29	Shane + Kast	2.″0	452/3306+300/7500	1865 (blue), 3 × 600 (red)
2019-11-07	30	Shane + Kast	2.″0	300/7500	1500 (red)
2019-11-21	43	Shane + Kast	2.″0	300/7500	2400 (red)
2019-11-26	48	Keck + LRIS	1.″0	600/400+400/8500	450 (blue), 438 (red)
2019-12-04	56	SOAR + Goodman	1.″0	400 m2	1200
2019-12-19	71	SOAR + Goodman	1.″0	400 m2	2 × 1320
2019-12-23	75	Shane + Kast	2.″0	452/3306+300/7500	2 × 1230 (blue), 4 × 600 (red)
2020-01-06	89	Shane + Kast	2.″0	452/3306+300/7500	1845 (blue), 3 × 600 (red)
2020-02-02	115	Shane + Kast	2.″0	452/3306+300/7500	1230 (blue), 2 × 600 (red)
2020-09-18	340	Keck + LRIS	1.″0	600/400+400/8500	910 (blue), 900 (red)

Pan-STARRS1 (PS1) template images (Flewelling et al. 2020) from each Swope *gri* frame.

Since we are not yet able to obtain a template image for the *u* band, we instead extracted photometry within a 5″ radius aperture and subtracted the host-galaxy light in *u* by modeling the host emission. The *u*-band emission of the host galaxy is estimated by fitting the PS1 photometry in the *grizy* bands and the 2MASS photometry in the *JHK* filters in a circular aperture of 5″ radius with the synthetic stellar population fitting code `PROSPECTOR`. Our best-fit continuity model of the star formation history with five age bins yields a stellar mass of $\log_{10}(M_\star/M_\odot) = 10.43 \pm 0.04$ and a metal content of $\log_{10}(Z/Z_\odot) = -1.11^{+0.22}_{-0.45}$, which are consistent with values derived by N20 and van Velzen et al. (2021).

2.2.3. LCO Photometry

We also obtained optical photometry of AT 2019qiz in the *ugr* bands from 2019 September 25 to November 27 with the Sinistro camera mounted on one of the 1 m telescopes of the LCO network in Siding Spring, Australia. Similar to our handling of the Swope photometry, we removed host-galaxy contamination by performing image subtraction for the *g* and *r* bands and by modeling the host flux in the same 5″ aperture for the *u* band.

2.3. UVOT Photometry

We extracted UV light curves from a series of 39 Swift UVOT observations with the package `HEASoft` v6.27 and CALDB version 20200305. We estimated the counts of the source from a circular aperture of 5″ radius and the background from a circular aperture of 40″ radius using the task `UVOTSOURCE`. These were then converted to flux and magnitude with the Swift photometric calibration data (Poole et al. 2008; Breeveld et al. 2011).

The Swift target-of-opportunity (ToO) observations covered the evolution of AT 2019qiz from $\Delta t = -11$ to 168 days. Although the observations were made in all six UVOT filters (*UVW2*, *UVM2*, *UVW1*, *U*, *B*, and *V*), in Figure 1 we only show the data from the three bluest filters (*UVW2*, *UVM2*, and *UVW1*), where the host-galaxy contributions are negligible. These are also the only Swift filters used in our data analysis. The nondetections in the archival GALEX All-Sky Imaging Survey place an upper limit of FUV > 20 mag and NUV > 20.8 mag on the host-galaxy light. Given that the flux in the Swift UV filters is highly dominated by the TDE at the time of the observations, we did not attempt to subtract the host-galaxy flux from these bands.

2.4. Optical Spectroscopy

We obtained a total of 18 spectroscopic observations with the Kast spectrograph (Miller & Stone 1993) on the Lick 3 m Shane telescope, the Goodman spectrograph on the SOAR telescope (Clemens et al. 2004), and LRIS on the Keck I 10 m telescope. Detailed instrumental configurations are listed in Table 1. We performed 1D spectrum extraction and flux calibration with standard `PyRAF`[15] routines. Observations of standard stars BD+174708 and BD+284211 were used to determine the relative flux calibration and remove telluric features (e.g., Foley et al. 2003; Silverman et al. 2012; Dimitriadis et al. 2019). All of the spectra presented in this paper have been corrected for Galactic extinction. We calibrated each spectrum's absolute flux by comparing its *g*-band synthetic photometry to the photometry from Swope and LCO imaging data (including host contribution), interpolated to each spectroscopic epoch.

3. Analysis

3.1. Black Hole Mass Estimation

We have not yet been able to obtain high-resolution spectra to measure the stellar velocity dispersion of the host galaxy. Nevertheless, N20 measured a velocity dispersion of $\sigma = 69.7 \pm 2.3$ km s^{-1} from their late-time X-shooter spectrum. Using the scaling relation derived for a sample of low-mass galaxies from Xiao et al. (2011), this velocity dispersion corresponds to a black hole mass of $\log_{10}(M_{\rm BH}/M_\odot) = 6.16 \pm 0.43$. Different M–σ relations generally agree with an upper limit of $\log_{10}(M_{\rm BH}/M_\odot) \lesssim 6.5$ (Nicholl et al. 2020). As detailed below, the black hole

[15] http://www.stsci.edu/institute/software_hardware/pyraf

Table 2
MOSFiT Best-fit Parameters

Parameter[a]	Value
$t_{\rm fallback}$ (days)	-25^{+1}_{-1}
$\log_{10} R_{\rm ph0}$	$0.9^{+0.06}_{-0.09}$
$\log_{10}(t_{\rm viscous}/{\rm days})$	$0.61^{+0.12}_{-0.29}$
$l_{\rm photo}$	$0.66^{+0.03}_{-0.03}$
β	$0.58^{+0.03}_{-0.03}$
$\log_{10}(M_{\rm BH}/M_\odot)$	$6.14^{+0.09}_{-0.1}$
$\log_{10}\epsilon$	$-3.47^{+0.13}_{-0.23}$
M_* ($M_\odot$)	$1.1^{+0.97}_{-0.1}$

Note.
[a] See Section 3.1 for parameter definition and Mockler et al. (2019) for detailed model description.

mass derived from light-curve fitting is also consistent with this value. Therefore we use $M_{\rm BH} = 1.4 \times 10^6\ M_\odot$ when estimating relevant scales throughout the paper.

We also used the Python package Modular Open-Source Fitter for Transients (MOSFiT; Guillochon et al. 2018) to simulate the observed UV and optical light curves in Figure 1 to derive the physical parameters of the TDE, including the black hole mass. The TDE model implemented in MOSFiT estimates the bolometric luminosity of the TDE by converting the mass fallback rates from hydrodynamic simulations (Guillochon & Ramirez-Ruiz 2013) with a constant efficiency parameter (Guillochon et al. 2018; Mockler et al. 2019). The program then tries to match the observed flux in each band by reprocessing the bolometric flux with a blackbody photosphere, assuming that the blackbody photosphere evolves as a power law of the mass fallback rate.

The TDE model in MOSFiT has eight parameters: black hole mass ($M_{\rm BH}$), stellar mass (M_*), scaled impact parameter (b), photosphere power-law exponent (l), photosphere radius normalization constant ($R_{\rm ph0}$), efficiency (ϵ), viscous delay time ($t_{\rm viscous}$), and the fallback time of the most bound debris ($t_{\rm fallback}$). We present the best-fit values from the MOSFiT run for AT 2019qiz in Table 2. The only constraint we imposed on the fitting parameters is for the stellar mass (M_*) to stay below $3\,M_\odot$. This is because M_* is not always well-constrained by MOSFiT owing to its degeneracy with the efficiency parameter, and it is physically unlikely for M_* to exceed $3\,M_\odot$ since higher-mass stars tend to have shorter lifetimes.

Our derived parameters are generally consistent with those of N20, though the fitting was performed on a different set of optical data. Our results suggest a negligible viscous time, therefore $t_{\rm fallback}$ approximates the start of the flare. We derived $t_{\rm fallback} = -25$ days relative to the time of peak light while N20 found $t_{\rm fallback} = -27$ days. This value is also consistent with that estimated from a photosphere expanding at constant velocity, where $\Delta t = -31 \pm 2$ days (see Section 3.2). The black hole mass of $\log_{10}(M_{\rm BH}/M_\odot) = 6.14 \pm 0.1$ derived from MOSFiT is in good agreement with that estimated from the M–σ relation.

3.2. Evolution of Blackbody Temperature, Radius, and Bolometric Luminosity

As a standard TDE analysis procedure, we model the spectral energy distribution (SED) of AT 2019qiz with a single-temperature blackbody. To do so, we first construct the SEDs at epochs having Swift observations in all three UV filters (*UVW2*, *UVM2*, and *UVW1*) and interpolate the photometry in the *ugri* filters measured from ground-based observatories. We show the best-fit blackbody temperature ($T_{\rm bb}$) and the 10%–90% confidence level in Figure 2. We derive the bolometric luminosity ($L_{\rm bol}$) at each Swift epoch by integrating over the best-fit blackbody spectra and calculate the emitting radius of the blackbody with the Stefan–Boltzmann law, where $L_{\rm bol} = 4\pi R_{\rm bb}^2 \sigma T_{\rm bb}^4$. The evolution of $L_{\rm bol}$ and $R_{\rm bb}$ is also given in Figure 2. Our measurements are in good agreement with those of N20.

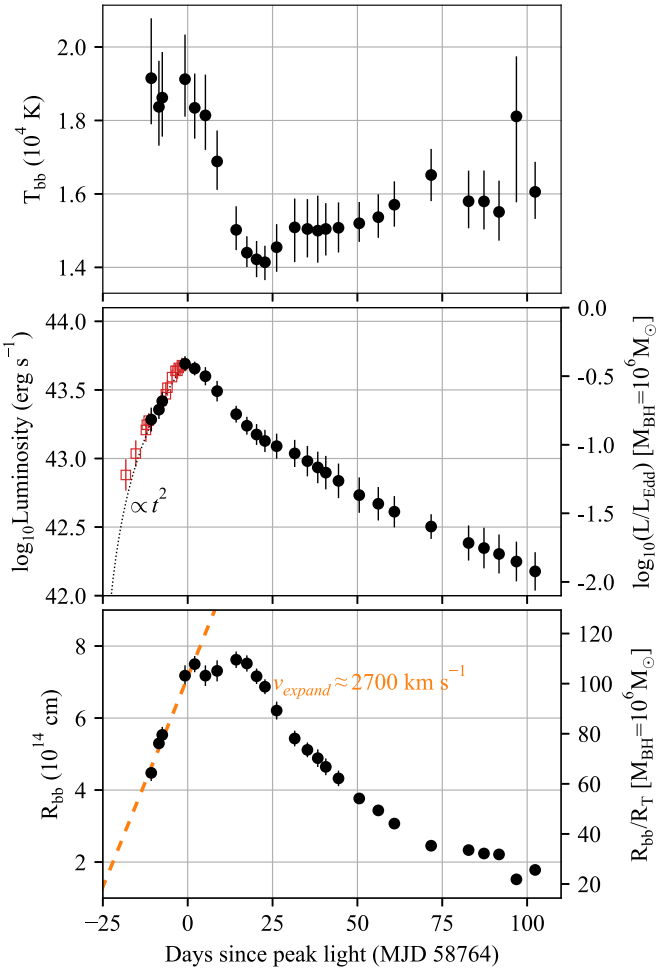

Figure 2. The evolution of blackbody temperature (top), bolometric luminosity (middle), and blackbody radius (bottom) measured from the UV and optical light curves at Swift epochs (black circles). We also show the luminosity scaled from the *r*-band light curve (open red squares) for the rising part to help visualize the early evolution. The dotted line in the middle panel shows the best-fit quadratic function to $L_{\rm bol}$ measured from the Swift epochs during the rise. The quadratic function asymptotically approaches a reference time $t_0 = -26.2$ days. The dashed orange curve displays the best-fit expansion velocity to the rising part of $R_{\rm bb}$.

The blackbody temperature of AT 2019qiz initially had a constant value of $T_{\rm bb} \approx 1.9 \times 10^4$ K as the light curves approached maximum brightness ($t_{\rm peak}$). From day 0 to day 25, it started to cool significantly down to $T_{\rm bb} \approx 1.4 \times 10^4$ K. Afterward, $T_{\rm bb}$ slowly recovered back to $\sim 1.6 \times 10^4$ K and remained roughly constant out to day 100. This initial decline in $T_{\rm bb}$ was also observed in ASASSN-14ae (Holoien et al. 2014) shortly after discovery around peak light, and in ASASSN-19bt while the light curves were rising (Holoien et al. 2019b). This cooling phase is short enough to be missed by previous TDE discoveries, where the classification and UV

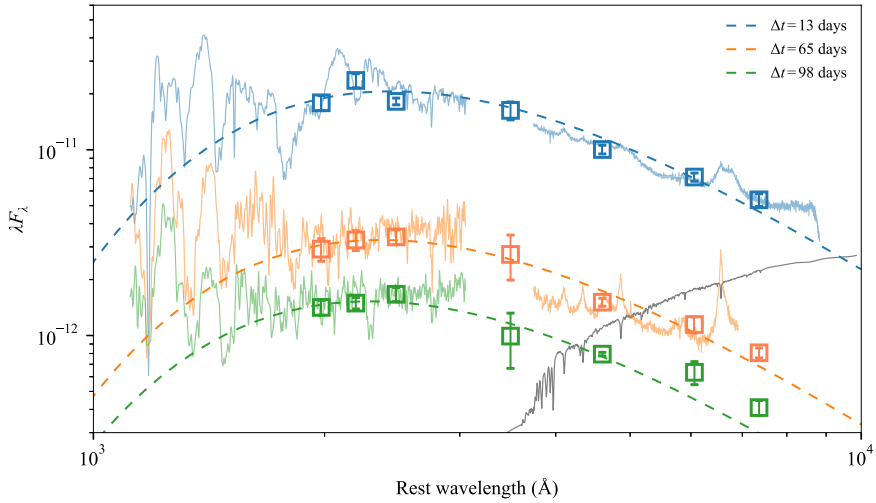

Figure 3. A sequence of HST UV spectra of AT 2019qiz, along with the UV and optical (*UVW2*, *UVM2*, *UVW1*, and *ugri*) photometry (squares) interpolated to the three HST epochs. Optical spectra obtained on $\Delta t = 13$ days (blue) and $\Delta t = 71$ days (orange) are also shown. The dashed lines mark the best-fit single-temperature blackbody ($T_{\rm bb} \approx 16{,}000$ K) to the interpolated UV and optical photometry at each epoch. The gray line shows the best-fit galaxy model from PROSPECTOR. As demonstrated here, a single-temperature blackbody can often underestimate the TDE continuum in the FUV.

follow-up observations typically came around or after maximum light; hence, only the constant-temperature phase was observed.

Our derived peak luminosity, $L_{\rm peak} = 4.9 \times 10^{43}$ erg s^{-1}, corresponds to an Eddington ratio of 0.27 assuming a black hole mass of $1.4 \times 10^6\ M_\odot$ estimated from the M–σ relation. We determine a total radiated energy of 1.3×10^{50} erg by extrapolating the luminosity linearly out to $t = \pm\infty$. If entirely powered by accretion, this energy would imply an accreted mass of $6.9 \times 10^{-4}(\epsilon/0.1)^{-1}\ M_\odot$, where ϵ is the accretion efficiency. The small accreted mass compared to the bound stellar mass could imply a low radiative efficiency or a partial disruption, or that we are underestimating the TDE energetics in other wavelengths (e.g., EUV or infrared). In fact, we see indications that the best-fit blackbody tends to underestimate the FUV continuum in our HST spectra. The luminosity evolution of AT 2019qiz places it in an unoccupied strip on the luminosity-phase plot that is between the "fast and faint" TDE iPTF16fnl and the slower but brighter TDE population (see Figure 1 of van Velzen et al. 2020 and Figure 10 of N20).

The blackbody radius increased monotonically with time toward light-curve peak. We estimate an expansion velocity of 2700 ± 200 km s^{-1} for the photosphere. It is worth mentioning that the derived photosphere expands at a much slower rate than the BALs ($\gtrsim$10,000 km s^{-1}) in the UV spectra, which suggests either a difference in the physical location of the outflow or that the two kinematic components are unrelated (see additional discussion in Section 4.1). If the photosphere was expanding at this constant velocity during the entire rise, this implies that the most bound debris fell back at $t_0 = -30.6$ days, which is well before the most recent ZTF preflare upper limit at $\Delta t = -21.7$ days. We estimated a similar reference time of -26 days by fitting the luminosity evolution during the rise time with a quadratic function $L \propto (t - t_0)^2$. The prediction of a quadratic rise traces back to the "fireball" model that is frequently used to describe the light curves of Type Ia supernovae (Riess et al. 1999). The TDE ASASSN-19bt, which has a densely sampled TESS rising light curve, also exhibits a power-law rise with an exponent of $\sim$2 (Holoien et al. 2019b).

3.3. Evolution of the UV Spectra

A sequence of three HST UV spectroscopic observations of AT 2019qiz is shown in Figure 3. Among the three HST epochs, the spectrum from the first epoch exhibits signatures distinct from those in previous TDEs. The apparent reduction in outflow velocity is also seen in the UV spectra for the first time. Below we describe these differences qualitatively and defer the quantitative details to the following subsections.

At all three epochs, high-ionization broad absorption lines (HiBALs) blueward of the rest wavelengths of N V, Si IV, and C IV can be readily seen. The HiBAL absorption troughs are blueshifted more in the first HST epoch ($v \approx 15{,}000$ km s^{-1} on $\Delta t = 13$ days) and decelerated to $v \approx 10{,}000$ km s^{-1} in the later two epochs ($\Delta t = 65$ and 98 days). In addition, the first HST spectrum is characterized by broad structures in the NUV ($\lambda_{\rm rest} \gtrsim 1650$ Å). We later identified these broad features to be associated with Al III λ1857 and iron (Fe II and Fe III) absorption, making AT 2019qiz the first TDE to be detected with Fe and low-ionization broad absorption lines (FeLoBALs). In fact, we find the BAL pattern in AT 2019qiz to share more similarities with that in a superluminous supernova (SLSN) than with those of BAL quasars (BALQSOs), which we discuss in more detail in Section 3.3.2.

At the first HST epoch, we also detect narrow absorption lines with a dispersion of 240 km s^{-1} at the host redshift $z_{\rm abs} \approx z_{\rm gal}$. The narrow absorption lines are only marginally detected at the later HST epochs owing to lower S/N. However, for the stronger absorption lines in the FUV, the line strengths do not seem to vary significantly between the first and second HST epochs.

3.3.1. Narrow Absorption Lines

We identified and measured the narrow absorption of both low- and high-ionization lines in the $\Delta t = 13$ days HST spectrum and tabulated them in Table 3. To interpret these narrow lines, we model them by defining the "effective continuum," which consists of the continuum emission and the broad TDE features (emission or absorption), and create a continuum-divided spectrum. This step is done by masking the

Table 3
Best-fit Parameters of Narrow UV Absorption Lines

Line	λ_0[a] (Å)	λ_{obs}[b] (Å)	FWHM (Å)	W_r[c] (Å)	z	log(gf)[d]	log(N/cm^{-2})[e]
Lyα	1215.67	1215.8	3.04 ± 0.16	2.39 ± 0.15	0.0152	−0.08	17.71
N V	1238.82	1238.72	2.1 ± 0.21	1.13 ± 0.14	0.015	−0.51	14.94
N V	1242.8	1242.51	2.55 ± 0.19	1.72 ± 0.15[f]	0.0149	−0.81	⋯
Si II	1260.42	1260.55	2.79 ± 0.25	1.74 ± 0.18	0.0152	0.29	15.12
Si II*	1264.73	1264.17	2.22 ± 0.66	0.45 ± 0.15	0.0146	0.55	⋯
O I	1302.17	1302.72	1.72 ± 0.19	0.63 ± 0.11[g]	0.0155	−0.62	⋯
Si II	1304.37	1304.72	1.72 ± 0.19	0.65 ± 0.11[g]	0.0154	−0.42	⋯
C II	1334.53, 1335.71	1335.07	2.12 ± 0.14	1.53 ± 0.13[g]	0.0155	−0.62	⋯
Si IV	1393.76	1393.83	2.23 ± 0.21	1.13 ± 0.13	0.0152	0.03	14.29
Si IV	1402.77	1402.94	2.3 ± 0.25	0.99 ± 0.13	0.0152	−0.28	14.29
Si II	1526.72	1526.53	1.77 ± 0.15	1.12 ± 0.12[f]	0.015	−0.59	⋯
C IV	1548.20	1547.73	3.04 ± 0.18	1.96 ± 0.20[g]	0.0148	−0.42	⋯
C IV	1550.77	1550.42	3.04 ± 0.18	2.35 ± 0.20[g]	0.0149	−0.72	⋯
He II	1640.42	⋯	⋯	⋯	⋯		
Al II	1670.79	⋯	⋯	⋯	⋯		
N III]	1750.26	⋯	⋯	⋯	⋯		
C III]	1908.00	⋯	⋯	⋯	⋯		
Fe II UV2	2344.21	2344.99	11.77 ± 0.55	2.84 ± 0.17[f]	0.0154	0.04	⋯
Fe II UV2	2374.0	2374.99	0.68	<0.06	0.0155	−0.55	⋯
Fe II UV2	2382.77	2383.86	3.9 ± 0.24	1.4 ± 0.11	0.0156	0.59	13.09
Fe II UV1	2586.65	2586.47	5.95 ± 0.61	1.04 ± 0.13	0.015	−0.19	13.63
Fe II UV1	2600.17	2601.24	6.06 ± 0.28	2.27 ± 0.13	0.0155	0.35	13.63
Mg II	2795.53	2797.34	5.13 ± 0.19	2.67 ± 0.12	0.0158	0.53	13.66
Mg II	2802.7	2804.44	3.0 ± 0.17	1.35 ± 0.09	0.0157	−0.21	13.66

Notes. From the $\Delta t = 13$ days HST spectrum. Absorption lines are modeled as individual Gaussian profiles after division by the local continuum.
[a] The rest wavelength of the line transition.
[b] The observed line center.
[c] The equivalent width of the line.
[d] Oscillator strength from the atomic spectral line database (Kurucz & Bell 1995).
[e] Column density.
[f] The transition may be subject to contamination by foreground absorption.
[g] Blended with neighboring lines in the same absorbing system. Therefore, we do not use the measured W_r to infer the metal column density.

parts of the spectrum containing narrow absorption lines, then smoothing and interpolating over the masked wavelengths that contain the narrow absorption lines using a Gaussian process with a squared exponential covariance function. We then divided the HST spectrum by this effective continuum, leaving only the narrow absorption features. Finally, we modeled these absorption lines with Gaussian profiles and measured their line widths and the equivalent widths (W_r) in the rest frame. Since the C IV $\lambda\lambda$1548, 1551 resonance doublet is not resolved in the spectrum, we modeled it by requiring the two components to have the same width. We also fix the width of O I λ1302 and Si II λ1304 to be the same due to line blending. The smoothed effective continuum, the normalized spectrum, and the best-fit models are shown in Figure 4. From the line fit, we measured an S/N-weighted velocity offset of 70 ± 90 km s^{-1} that is consistent with the systemic host velocity using only the isolated and unblended absorption lines. We further place an upper limit of $\lesssim$200 km s^{-1} on the outflow velocity based on the weak Si II λ1265 feature. The average dispersion of the absorption lines is 240 ± 70 km s^{-1}.

We adopt the multi-ion single-component curve of growth (CoG) analysis to derive the ionic column densities from the measured W_r of the narrow absorption lines assuming that the Doppler broadening parameter b is the same for each ionic species. This assumption holds if all the absorption, regardless of high- or low-ionization lines, took place in a relatively small region that cannot be resolved by our HST spectrum. We solve for b iteratively using the unsaturated, unblended ionic lines with the same lower energy states (Si IV, Fe II UV1, and Mg II). In our best-fit model (Figure 5), $b = 95$ km s^{-1}. The column densities for the uncontaminated and unblended ionic species are listed in Table 3.

We note that one caveat of applying the CoG analysis to a low-resolution spectrum, such as our STIS observation, is that the derived metal column densities can be underestimated by as much as 1 dex (Prochaska 2006). High-quality and high-resolution spectroscopy of the afterglows of gamma-ray bursts (GRBs) suggests that the absorption-line structures around strong Fe II lines are characterized by multiple saturated components spreading over a few hundred km s^{-1}. In lower-resolution spectra, these absorption structures may be viewed as a single component with greater effective b. Although the larger b value does not necessarily lead to erroneous inference of the column density, it can sometimes affect the measurements by forcing weaker transitions to be optically thin ($\tau_0 \propto b^{-1}$) even when they are saturated. Fine structures may also be present in the absorption lines in AT 2019qiz. Therefore, we emphasize that the metal column densities displayed in Table 3 should be considered as lower limits.

3.3.2. Identification of the UV Broad Lines

Before delving into the identification of broad features in AT 2019qiz, we remind readers that the continuum placement,

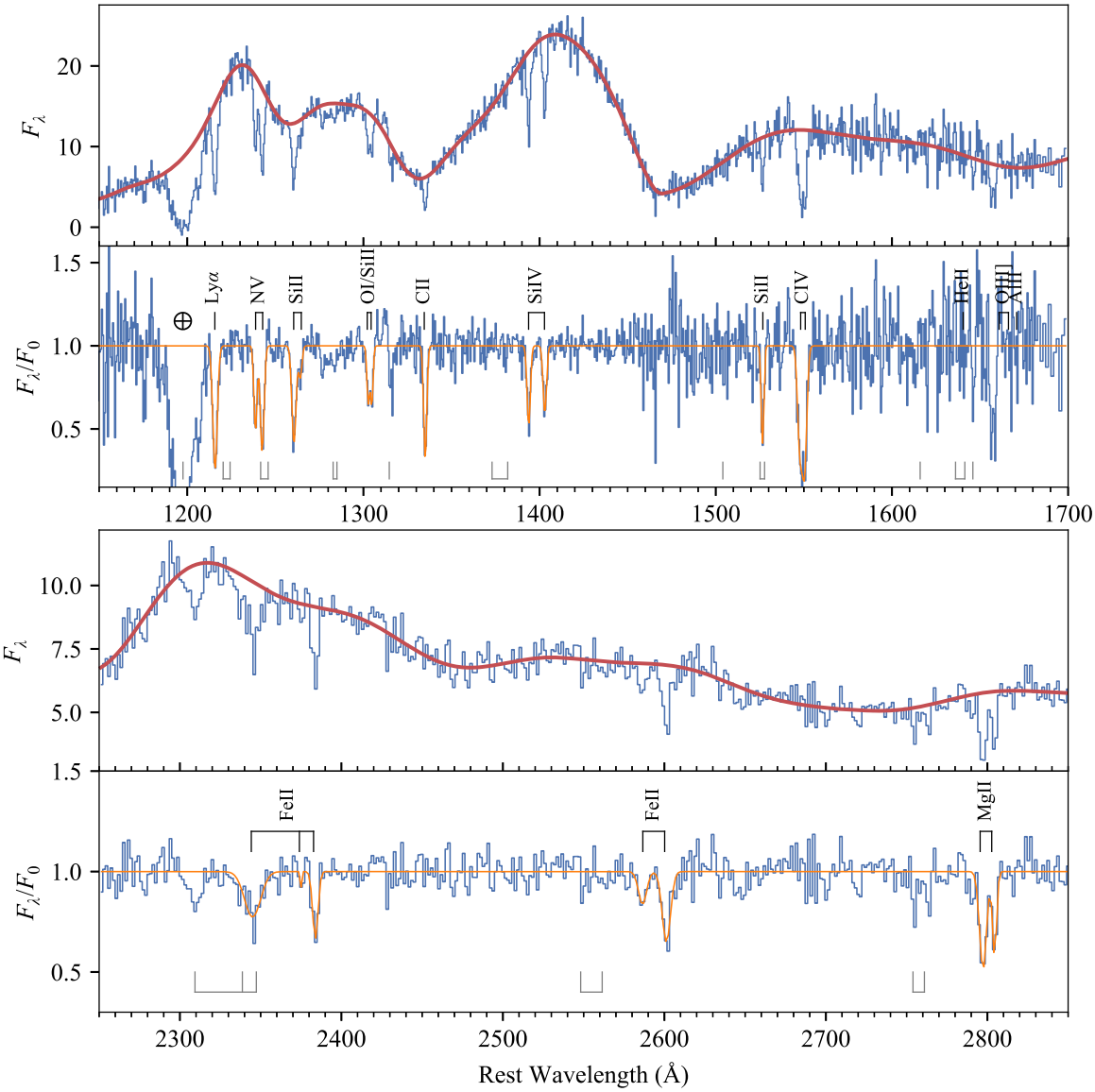

Figure 4. Narrow absorption lines in the HST FUV (top) and NUV (bottom) spectra on $\Delta t = 13$ days. For each wavelength segment, the original spectrum (blue) and the smoothed effective continuum (red) are shown in the upper panel while the normalized spectrum is shown in the lower panel. We identified the line transitions (labeled in black) and modeled the normalized narrow absorption lines with Gaussian profiles, where the best-fit models are shown in orange. In the panels with normalized spectra, the gray ticks mark the wavelengths of common Galactic absorption lines.

especially in the FUV, may be quite uncertain. Traditionally, we find that the NUV and optical photometry can be described well by a single-temperature blackbody with $T_{\rm bb} \approx$ a few $\times$ 10^4 K. This has been confirmed to be generally true by past HST observations, where the NUV spectra of most TDEs are characterized by a featureless continuum with a slope that is consistent with the Swift photometry in each event (Cenko et al. 2016; Brown et al. 2018; Blagorodnova et al. 2019; Hung et al. 2019). At $\lambda_{\rm rest} < 1600$ Å, the common presence of HiBALs often obscures a large amount of flux in the FUV continuum and broad emission lines in TDEs, making the FUV continuum placement especially difficult. It is noticed that the FUV continuum can be significantly underestimated by extrapolating the NUV blackbody spectrum, as was found in AT 2018zr (Hung et al. 2019) and also in AT 2019qiz (Figure 3). Therefore, in the analysis we avoid measuring line properties that are dependent on the continuum, such as the line flux or balnicity index (BI; a measure of the strength of the BAL features defined in Weymann et al. 1991), except for the narrow absorption lines, where the effective continuum can be determined relatively accurately.

Despite the fact that the blackbody spectrum extrapolated from NUV and optical observations is clearly underestimating the FUV continuum, we keep them in Figure 3 to guide the eye. Broad emission and absorption features are detected at all three epochs. In order to identify the lines, it is natural to compare the HST spectra of AT 2019qiz with a BALQSO since both TDEs and BALQSOs are phenomena driven by accretion and winds. Furthermore, similarities between the rest-frame UV spectra of TDEs and BALQSOs have been drawn in the past (e.g., Blagorodnova et al. 2019). We find broad structures in both the FUV and NUV sides of the spectrum on day 13. Broad emission lines seem to have formed around the rest wavelengths of the high-ionization lines N V, Si IV, and C IV. Blueward of these emission lines are the absorption troughs associated with these high-ionization transitions. We estimate

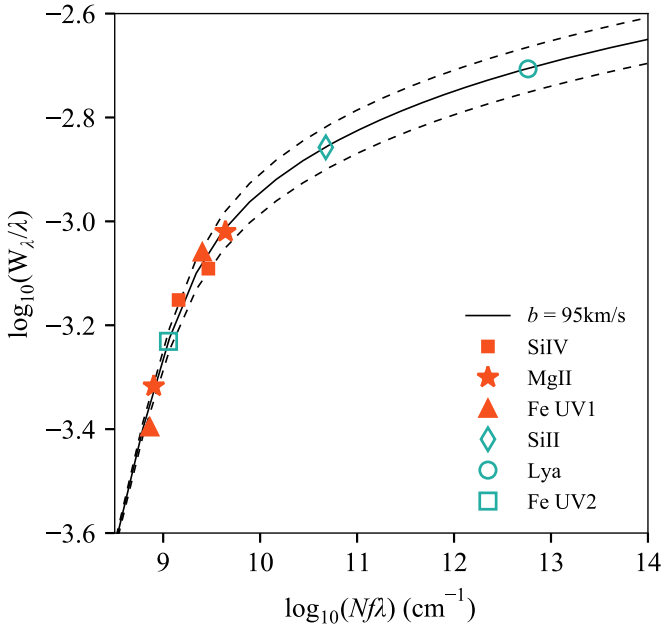

Figure 5. The best-fit CoG curve with $b = 95$ km s^{-1} is shown by the black solid curve. The dashed curves mark the ± 10 km s^{-1} uncertainty in b. Unblended transitions with multiple components used to constrain the fit are marked by red solid symbols. We interpolate the ionic column density for spectral lines with only a single measured component (green open symbols) to the best-fit curve.

the blueshift velocity of the broad absorption features (v_w) with respect to the minimum of the troughs. The broad features associated with Si IV and C IV are blueshifted by $v_w \approx 15{,}000$ km s^{-1}, whereas the velocity offset of the N V absorption trough cannot be precisely measured owing to overlap with the geocoronal emission.

A subclass of BALQSOs, the low-ionization broad absorption line (LoBAL) QSOs, have UV spectra imprinted by broad absorption of Mg II $\lambda\lambda$2796, 2803, Al III, and Al II at $\lambda_{\rm rest} > 1750$ Å. In even rarer cases, iron absorption lines are present in the QSO spectra, and thus these QSOs are termed "FeLoBAL" QSOs. Given the presence of similar ionic species, we compare AT 2019qiz with the spectrum of an SDSS FeLoBAL QSO at $z \approx 2.1$ in Figure 6. From this comparison, we infer that the absorption around 1800 Å in AT 2019qiz is likely due to a blueshifted ($v_w \approx 9000$ km s^{-1}) Al III λ1857 line. At $\lambda_{\rm rest} > 2000$ Å, the $\Delta t = 13$ days spectrum of AT 2019qiz is characterized by several broad peaks and valleys around the most prominent Fe II and Fe III lines. The iron lines that are possibly associated with the broad NUV features are labeled by dashed lines in Figure 6. If we attribute the absorption features at 2000 and 2240 Å to Fe III and Fe II UV2, the measured wavelengths correspond to $v_w \approx 12{,}000$–$16{,}000$ km s^{-1}, which is in good agreement with that derived from the HiBALs. Unlike the BALQSOs, the HST spectra of AT 2019qiz did not show any significant broad, blueshifted Mg II $\lambda\lambda$2796, 2803 absorption at any phase (Figure 6).

Intriguingly, we find the $\Delta t = 13$ days UV spectrum of AT 2019qiz to bear greater resemblance to the SLSN Gaia16apd (Yan et al. 2017) than to any type of BALQSOs (Figure 6). The similarity between the two spectra possibly stems from the fact that both events had a similar blackbody temperature ($T_{\rm bb} \approx 17{,}000$ K) and an expanding photosphere, as probed by the SED fit in Section 3.2, during the early phases. The absorption troughs at 1750 Å $< \lambda_{\rm rest} <$ 2400 Å aligned particularly well with Gaia16apd after redshifting the SLSN spectrum by 12,000 km s^{-1}. Using the `syn++` model that generates synthetic spectra for homologously expanding atmospheres, Yan et al. (2017) identified the ionic species that contribute to each absorption line in Gaia16apd. This new comparison makes a difference in the identification of the features at 1800 and 2240 Å. If the ionization state is also similar in AT 2019qiz and Gaia16apd, the 2240 Å feature would instead be attributed to the absorption of C II with $v_w \approx 11{,}000$ km s^{-1}. In addition, the 1800 Å feature would not be uniquely associated with Al III, but also with Si II and Ti II. The absorption troughs around the Si IV and C IV lines may also be contributed by other low-ionization species such as C II and Si II. While many LoBALs are detected in the day 13 UV spectrum, the lack of Mg II $\lambda\lambda$2796, 2803 in AT 2019qiz would possibly need to be explained by the composition.

The broad UV features evolved significantly from day 13 to day 65. The most remarkable difference is that the absorption troughs associated with the high-ionization Si IV and C IV $\lambda\lambda$1548, 1551 lines became redder, decelerating from $v_w \approx 15{,}000$ km s^{-1} to $v_w \approx 10{,}000$ km s^{-1} (Figure 7). We also notice that the NUV spectrum became featureless and the UV spectra resemble those of previously observed TDEs more at later epochs. The spectra of day 65 and day 98 are very similar except that the bluest Si IV absorption edge seems to have moved to a slightly lower velocity on day 98 (Figure 7).

3.4. Optical Spectroscopic Analysis

We show a sequence of 18 optical spectra of AT 2019qiz in Figure 8. The spectroscopic features in AT 2019qiz underwent significant changes on a timescale of days to weeks. This is best illustrated by the evolution in the shape of the Hα emission (Figure 9). The pre-peak and early post-peak spectra from day −13 to day 13 are characterized by a blue continuum with very broad emission features around Hα and He II λ4686. The latter is likely contaminated by the emission from Hβ because the entire broad feature spans rest wavelengths 4400–5200 Å. During this stage, the Hα emission structure has an FWHM intensity of 2.6×10^4 km s^{-1}. We fit this broad Hα feature with a double Gaussian function and derived two components with similar FWHMs of $\sim 1.5 \times 10^4$ km s^{-1} centered roughly at the rest wavelength of Hα and at a redshift of 1.6×10^4 km s^{-1}. The red component has a weaker line flux, about half that of the blue component.

On day 22, the Hα emission-line profile changed dramatically, with a narrow component appearing around the rest-frame Hα wavelength. We then modeled the Hα emission with three Gaussians simultaneously while requiring the narrow component to have FWHM < 6000 km s^{-1}. The best-fit model consists of a broad Hα base, which is the sum of two Gaussians as in the earlier epochs, with FWHM of 2.1×10^4 km s^{-1} and a narrow Hα component with FWHM of 3000 km s^{-1} centered at zero velocity. During this time, the blue and red components of the broad Hα emission became almost equally strong while the velocity offset of the red component decreased to 1.1×10^4 km s^{-1}.

The broad Hα base continues to decay while the narrow Hα remains strong in all later epochs. The broad Hα showed not only showed a decrease in line flux but also a change in the line shape. From day 71 onward, the broad Hα shifted to a single Gaussian centered around the rest Hα wavelength, where the red shoulder detected with $v > 10{,}000$ km s^{-1} at previous

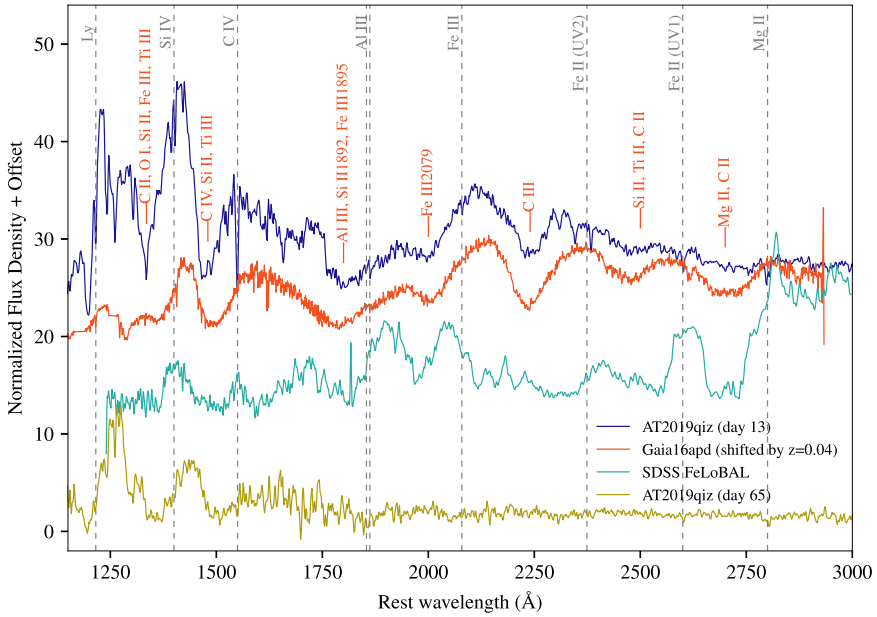

Figure 6. UV spectra of AT 2019qiz on day 13 and day 65, compared to the SLSN Gaia16apd (Yan et al. 2017) and the FeLoBAL QSO SDSS J090152.04+624342.6 (Wang et al. 2017). The first UV spectrum of AT 2019qiz bears a stronger resemblance to that of Gaia16apd. The orange labels mark the potential contributing species identified by Yan et al. (2017).

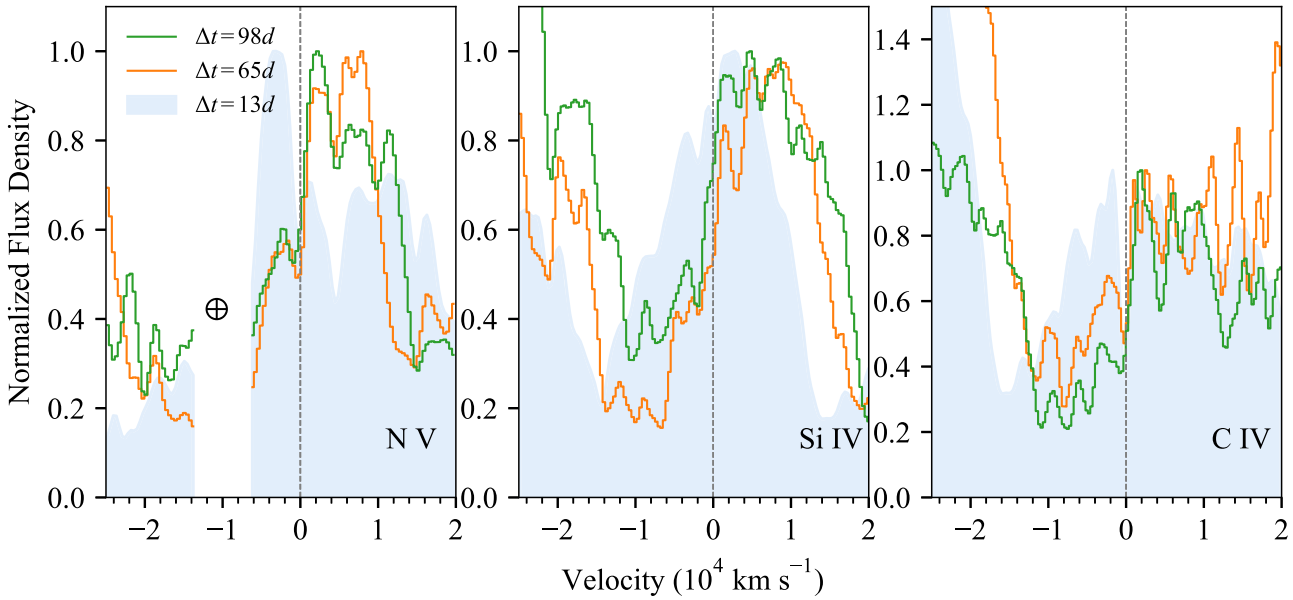

Figure 7. Three epochs of HST STIS spectra in velocity space with respect to the rest wavelengths of the high-ionization lines N V, Si IV, and C IV. The region affected by geocoronal airglow emission indicated by a circled plus symbol is truncated. The UV spectrum from the first HST epoch ($\Delta t = 13$ days) is shaded in pale blue while the spectra from the second and the third epochs are plotted as orange and green curves, respectively. It can be seen that the absorption troughs shifted to lower velocities as time progressed from 13 to 65 days, which makes the emission lines seem more redshifted.

epochs disappeared. The FWHM of the broad Hα dropped to $\sim$12,000 km s^{-1}. The FWHM of the narrow Hα emission fluctuates between 3000 and 4000 km s^{-1} since it first appeared around day 22.

Narrow Balmer emission lines from higher excited states and narrow Bowen emission (He II + N III) likely also appeared from day 22 onward. However, only after day 49 did the broad emission and continuum fade enough for the narrow lines to be detected. The presence of both the Balmer lines and He II + N III makes AT 2019qiz a TDE-Bowen, which is a spectral class that makes up about half of the optical TDE population defined by van Velzen et al. (2021). On day 71, when the narrow emission lines are the strongest, we measured an FWHM of 4000 km s^{-1} for Hβ and an FWHM of 3100 km s^{-1} for Hγ. The line intensity ratio Hα/H$\beta \approx 1.2$ corresponds to a flat Balmer decrement, which has also been reported in several TDEs (e.g., AT 2018hyz; Hung et al. 2020; Short et al. 2020). We also measured intensity ratios Hγ/H$\beta \approx 0.6$ and (He II + N III)/H$\beta \approx 1$.

3.5. Host Galaxy and the X-Ray Emission

The host galaxy of AT 2019qiz is 2MASX J04463790–1013349 (WISEA J044637.88–101334.9) at $z = 0.0151$. The r-band Pan-STARRS image reveals that it is a spiral galaxy with a clear bar

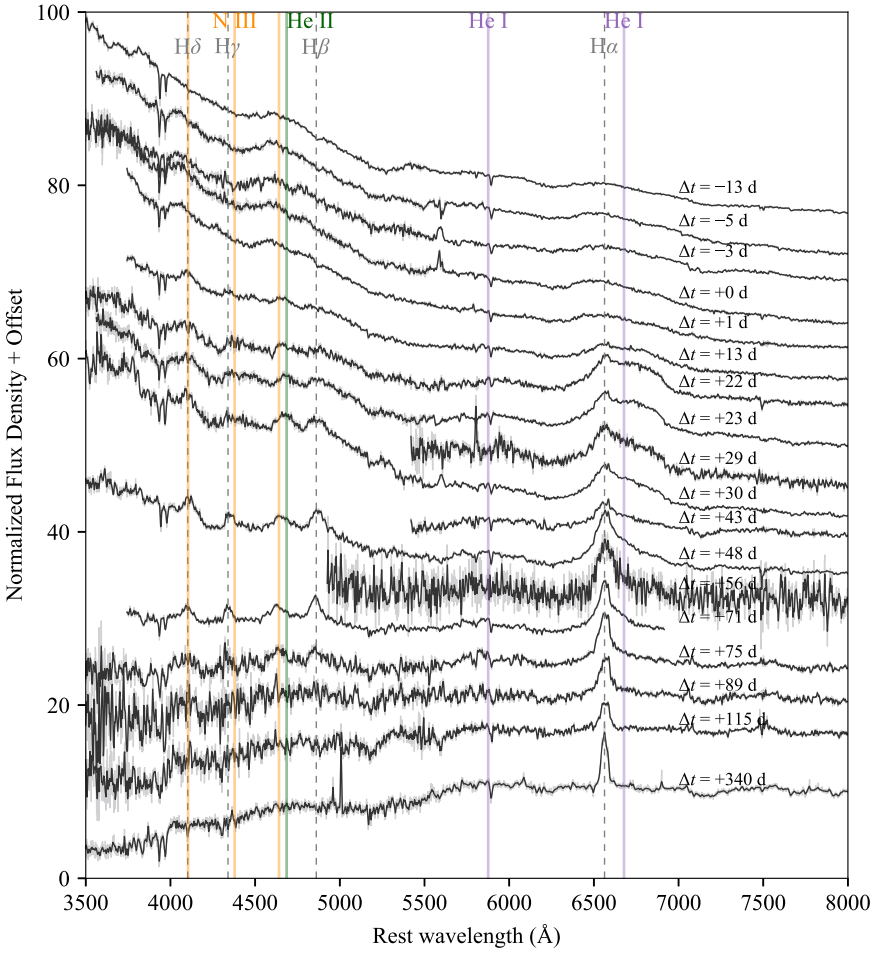

Figure 8. Optical spectra of AT 2019qiz obtained between $\Delta t = -13$ days and $\Delta t = 340$ days. The spectra smoothed by a Gaussian kernel with $\sigma = 2$ Å are shown by black lines while the original data are shown by gray. The gray dashed lines mark the wavelengths of the Balmer series. Colored vertical lines mark the wavelengths of N III (orange), He II (green), and He I (purple). Significant line-profile evolution is seen in the Hα emission.

structure. N20 measured a Sérsic index in the range 5.2–6.3, which is considered high compared to the galaxy sample in the same black hole mass bin (Law-Smith et al. 2017). Like many other TDEs, AT 2019qiz is in a galaxy with a more concentrated population of stars (French et al. 2020).

In the late-time optical spectra of AT 2019qiz, we detect nebular emission lines [O III] $\lambda\lambda$4959, 5007 and [N II] $\lambda\lambda$ 6548, 6583 that are indicative of preflare activity in an active galactic nucleus (AGN). Given that the TDE light has faded substantially in the $\Delta t = 340$ days spectrum, we fit its stellar and gas kinematics simultaneously using the Penalized Pixel-Fitting (pPXF) package (Cappellari 2017) with the MILES stellar library (Figure 10). In addition to the narrow nebular emission lines, we added a second gas component in our fit to account for the TDE Balmer emission at late times, which has also been observed in previous TDEs (e.g., AT 2018zr; Hung et al. 2019). Our best-fit width for the TDE Balmer lines (FWHM ≈ 2000 km s^{-1}) is consistent with the width of the narrow Hα component in earlier TDE spectra (22 days $\leqslant \Delta t \leqslant 115$ days). We measured the flux of the host-galaxy emission lines and plot the line ratios in a Baldwin, Phillips, & Terlevich (BPT) diagram (Baldwin et al. 1981) (Figure 10). The line ratios are in good agreement with the nebular emission lines being produced by AGN photoionization.

During the flare, N20 measured a weak X-ray luminosity of $L_X = 5.1 \times 10^{40}$ erg s^{-1} in AT 2019qiz that is 2–3 orders of magnitude below the UV and optical luminosity. N20 associated the X-ray emission with the TDE rather than the AGN owing to variability in the X-ray flux and the evolution of the hardness ratio. However, the hardness ratio of -0.1 ± 0.04 from the merged XRT observations is at the higher end of the TDE distribution when compared to X-ray-bright TDEs such as ASASSN-14li, and is more similar to those seen in AGNs (Auchettl et al. 2018). Therefore, the possibility of AGN-driven X-ray emission in AT 2019qiz cannot be completely ruled out.

4. Discussion

4.1. Photosphere Evolution

The UV and optical photometry reveals the evolution of the blackbody radius from the pre-peak phase out to $\Delta t \approx 100$ days. The blackbody radius was initially expanding linearly with a velocity of 2700 km s^{-1} up to the time of peak light in the UV and optical. The constant-velocity phase was then followed by a constant-radius phase for $\sim$25 days before the radius began to shrink with time like that observed in previous TDEs, as a result of the combination of decreasing luminosity and constant color temperature.

Our intensive follow-up observations of the optical photosphere and the BALs in the UV spectra strongly support the presence of an outflow that evolved significantly with time in AT 2019qiz. Various models have been proposed to explain the

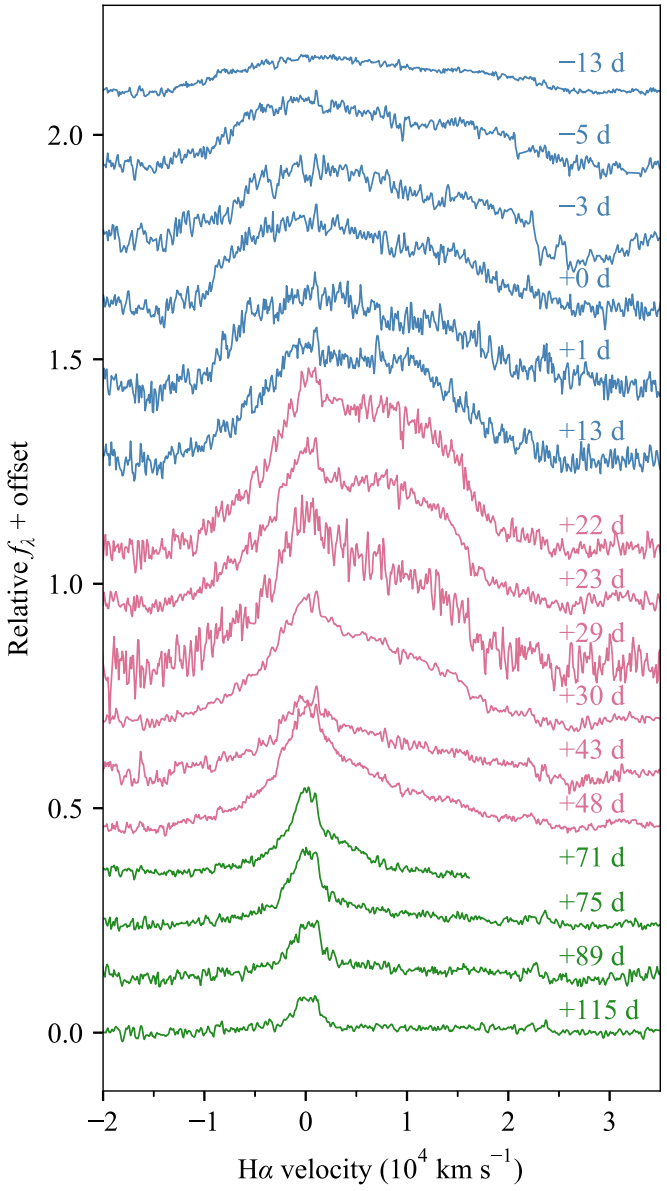

Figure 9. Evolution of the Hα emission profile after continuum subtraction. We used models with different numbers of Gaussian components to fit the line at different phases. The Hα line profile in the earliest spectra can be characterized by two broad Gaussians (blue). In the post-peak period, a narrow component became apparent, which motivated us to adopt a three-component model (pink) to describe the line shape. In later spectra, the red shoulder in the broad Hα disappeared; thus, we use a narrow and a broad component centered around Hα to model the emission line (green).

origin of TDE outflows (Strubbe & Quataert 2009; Lodato & Rossi 2011; Dai et al. 2018; Lu & Bonnerot 2020). In such models, the wind typically has a nonspherical configuration, and the velocity can have some variation depending on the wind-launching radius and observer inclination. However, when strong optical emission is observed, one can assume that the wind is mass-loaded and optically thick along the line of sight, thus justifying the adoption of a quasispherical model for studying the wind physics (Metzger & Stone 2016; Roth et al. 2016). Here we construct a simple 1D wind model, where the mass outflow rate is $\dot{M}_{\rm wind} = 4\pi r^2 \rho_{\rm wind} v_{\rm wind}$, based on the observed results. The photospheric radius ($R_{\rm ph}$) corresponds to the surface of electron scattering where the optical depth is $\tau_e \propto \rho(r = R_{\rm ph}) R_{\rm ph}$. By definition, $\tau_{\rm e} = 2/3$. Therefore, $R_{\rm ph}$ should be proportional to the mass outflow rate divided by the wind velocity, $R_{\rm ph} \propto \dot{M}_{\rm wind}/v_{\rm wind}$. If we assume that the observed luminosity scales roughly linearly with the accretion rate $\dot{M}_{\rm acc}$, then from the three UV BAL velocity measurement at $\Delta t = 13$, 65, and 98 days post-peak, we can derive a scaling relation $v_{\rm wind} \propto \dot{M}_{\rm acc}^{0.2}$. Putting this together with the observed evolution of photosphere radius $R_{\rm bb} \propto \dot{M}_{\rm acc}^{0.6}$ during these times, we can constrain that $\dot{M}_{\rm wind} \propto \dot{M}_{\rm acc}^{0.8}$. This is consistent with the results of Strubbe & Quataert (2009) and Lodato & Rossi (2011), stating that a stronger wind is launched at earlier phases in TDEs when the mass fallback rate is higher.

In the analytical model developed by Metzger & Stone (2016), only a small fraction of the bound debris accretes onto the black hole. The binding energy of the accreted mass naturally gives rise to a quasispherical outflow that is massive enough to absorb and reprocess the hard EUV/X-ray photons into UV and optical emission. One prediction of the model of Metzger & Stone (2016) is that the TDE light curve can deviate from the mass fallback rate ($\propto t^{-5/3}$) at early times owing to photon trapping. They find that the observed luminosity can be suppressed at first because of adiabatic losses in the inner wind, resulting in a flatter light curve than $\propto t^{-5/3}$. The suppression continues until the trapped photons are advected to a radius where the photon diffusion time is short compared to the outflow expansion time on a timescale of $t_{\rm tr}/t_{\rm fallback} \approx 2.6 \beta^{3/5} M_{\rm BH}^{-1/2} m_\star^{1/5} R_{\rm in,6}^{-3/5}$. At this point, photons can diffuse out of the ejecta freely and thus allow the photosphere to cool. The effect of photon trapping aligns with the observed $T_{\rm bb}$ evolution of AT 2019qiz, where the measured temperature started to decrease at around one fallback time. This may also explain why the cooling in ASASSN-14ae and ASASSN-19bt occurred at different phases, since the trapping time is dependent on other parameters.

The balance between decreasing luminosity and decreasing temperature gives rise to the plateau in the blackbody radius from $\Delta t = 0$ to 25 days. In practice, the photosphere velocity does not need to follow the outflow velocity if the density or ionization of the photosphere is changing. That is, even if the gas producing the UV and optical continuum continues to expand at a constant velocity, a reduction in the electron density can move the electron-scattering photosphere inward, and can lead to a plateau or even a decrease in the derived blackbody radius as observed in AT 2019qiz.

4.2. TDE UV Spectra

Blueshifted broad absorption features detected in AT 2019qiz signify the presence of outflowing gas at a phase as early as $\Delta t = 13$ days. The ejecta producing the BALs would have reached a distance of $\sim 5 \times 10^{15}$ cm if they were moving at the same velocity since the most bound debris returned to the pericenter (assuming $t_{\rm fallback} = -25$ to -30 days). BALs have also been detected at different stages in almost all of the TDEs observed with UV spectroscopy, including PS1-11af, iPTF15af, iPTF16fnl, and AT2018zr (Chornock et al. 2014; Brown et al. 2018; Blagorodnova et al. 2019; Hung et al. 2019). Among the HST TDE sample, ASASSN-14li is the only object that exhibits pure broad emission lines (Cenko et al. 2016).

To date, iPTF16fnl ($\Delta t = 7$, 22, 44 days), AT 2018zr ($\Delta t = 23$, 36, 41, 59, 62 days), and AT 2019qiz ($\Delta t = 13$, 65, 98 days) are the only TDEs with a sequence of HST UV

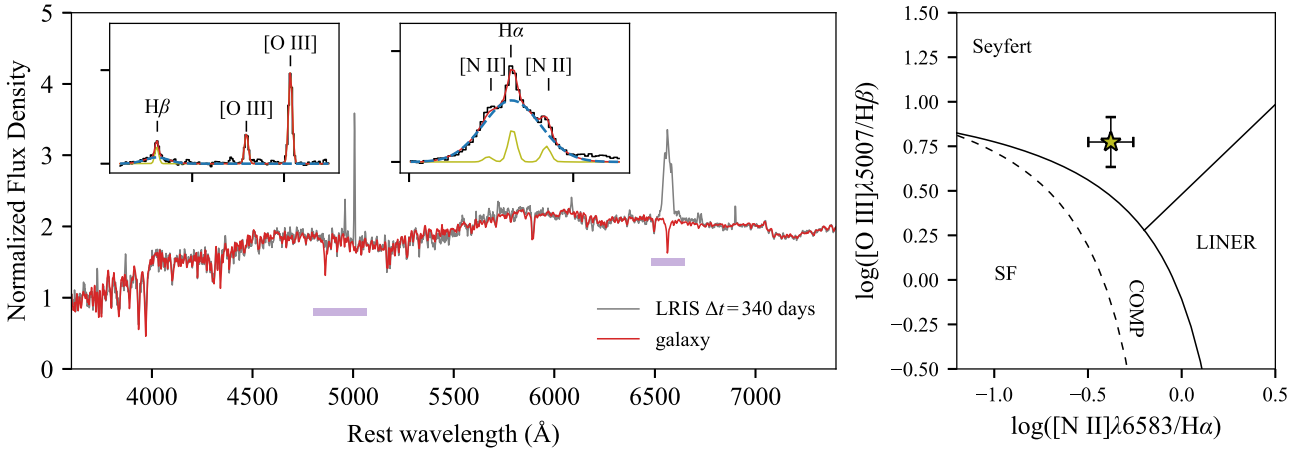

Figure 10. Left: late-time Keck spectrum of AT 2019qiz (gray) overlaid with the best-fit host-galaxy model (red) with pPXF. We fit the stellar population as well as the host and TDE emission lines simultaneously. The emission-line spectrum (host-subtracted) around Hα and Hβ are shown in the insets, where the TDE emission is marked by blue dashed lines and the host emission is plotted in yellow. Right: the BPT emission-line diagnostic diagram. The narrow-line ratios of the host galaxy of AT 2019qiz fall in the region occupied by AGNs.

spectra (Brown et al. 2018; Hung et al. 2019). Among these, AT 2019qiz has the longest observational baseline. Each of these TDEs follows a very different evolutionary path. In the earliest HST epoch, iPTF16fnl was observed with weak HiBALs (FWHM $\approx 6000\,\mathrm{km\,s^{-1}}$) that diminished over time. AT2018zr started resembling ASASSN-14li with a UV spectrum characterized by broad emission lines. Broad absorption troughs blueward of both high- and low-ionization species with a velocity offset of $\sim 0.05c$ started to appear from day 59 onward. AT 2019qiz exhibited a rare FeLoBAL spectrum at the first epoch, which then transitioned into a HiBAL spectrum at the two later epochs. The HiBALs remained strong in AT 2019qiz though the outflow velocity decreased from 15,000 to 10,000 $\mathrm{km\,s^{-1}}$ in $\sim$50 days (Figure 7). The decrease in outflow velocity is consistent with the theoretical prediction, where the wind becomes weaker with time as the mass fallback/accretion rate declines.

We select the most representative phases from the multi-epoch HST spectra of iPTF16fnl, AT2018zr, and AT2019 qiz and compare them with the single-epoch spectra obtained for all the rest of the TDEs shown in Figure 11. While we arrange the spectra in Figure 11 with respect to phase, we find that any two spectra obtained at comparable phases do not guarantee similarity.

The spectrum that stands out in the current UV TDE population is the UV spectrum of AT 2019qiz at $\Delta t = 13$ days (Figure 11). The presence of FeLoBALs in the UV spectrum of AT 2019qiz is in accordance with the reprocessing scenario. Photoionization models of FeLoBAL QSOs, which are typically X-ray-faint, suggest that high column densities are required in order to produce the iron features (e.g., $N_{\mathrm{H}} \approx 10^{20.6}\,\mathrm{cm^{-2}}$; Korista et al. (2008)). Analogously, the BAL clouds need to be shielded from the hard X-ray photons to form the FeLoBAL in AT 2019qiz. The shielding gas may be an inner wind consisting of material that has fallen back more recently, as proposed in the model of Metzger & Stone (2016). In a few fallback times, the column density drops sufficiently low such that the ejecta become transparent to the X-ray and EUV photons. This likely explains why the iron and low-ionization features disappeared, leaving only the HiBALs in later HST spectra of AT 2019qiz.

As shown in Figure 6, this spectrum is more like that observed in SLSNe instead of in TDEs or BALQSOs. According to the model of Metzger & Stone (2016), the outflow properties of TDEs may be similar to those in engine-driven supernovae as black hole accretion continues to inject energy into the ejecta. The observed similarities between the early-time UV spectral features in AT 2019qiz and those in the SLSN Gaia16apd are strong evidence supporting this connection.

The HiBAL TDE spectra, which are seen in at least half of the TDEs at a later phase, all seem to be very similar except for small differences in outflow velocities (6000–15,000 $\mathrm{km\,s^{-1}}$). The reduction in the mass fallback rate and the expanding ejecta likely facilitated changes in the ionization structure and the column densities that cause the UV spectral features to transition from SLSN-like to more BALQSO-like. It is worth noting that the C IV and Si IV emission always appears to be weaker than the N V emission in TDEs while the same trend is not observed in AGNs and BALQSOs. This may be attributed to the stellar debris having a higher N/C ratio owing to CNO processing in the stellar core (Cenko et al. 2016; Kochanek 2016; Yang et al. 2017; Gallegos-Garcia et al. 2018; Law-Smith et al. 2019, 2020).

The diverse properties of the TDE UV spectra perhaps reflect the intricate processes involved in a TDE, such as accretion disk formation and wind launching. In recent theoretical developments, studies have shown that orientation effects can, at least in part, explain the diverse broadband and line-emission/absorption properties seen in TDEs (Dai et al. 2018; Parkinson et al. 2020).

Parkinson et al. (2020) simulated spectra with broad emission lines (BELs) and BALs with a disk and wind model for TDEs. In particular, they rendered spectra that consist of purely BELs on sightlines that do not intersect the disk wind. While viewing angle may be responsible for the dichotomy of BELs and BALs in TDE spectra, it does not explain how one object can transition from BEL to BAL, as seen in AT 2018zr during the first 60 days (Hung et al. 2019). The SLSN-like early-time spectrum of AT 2019qiz further calls for a time-dependent, multizone wind model to be considered in future TDE simulations. Including AT 2019qiz, the high occurrence of BALs in TDE spectra (c.f. QSOs) continues to support a

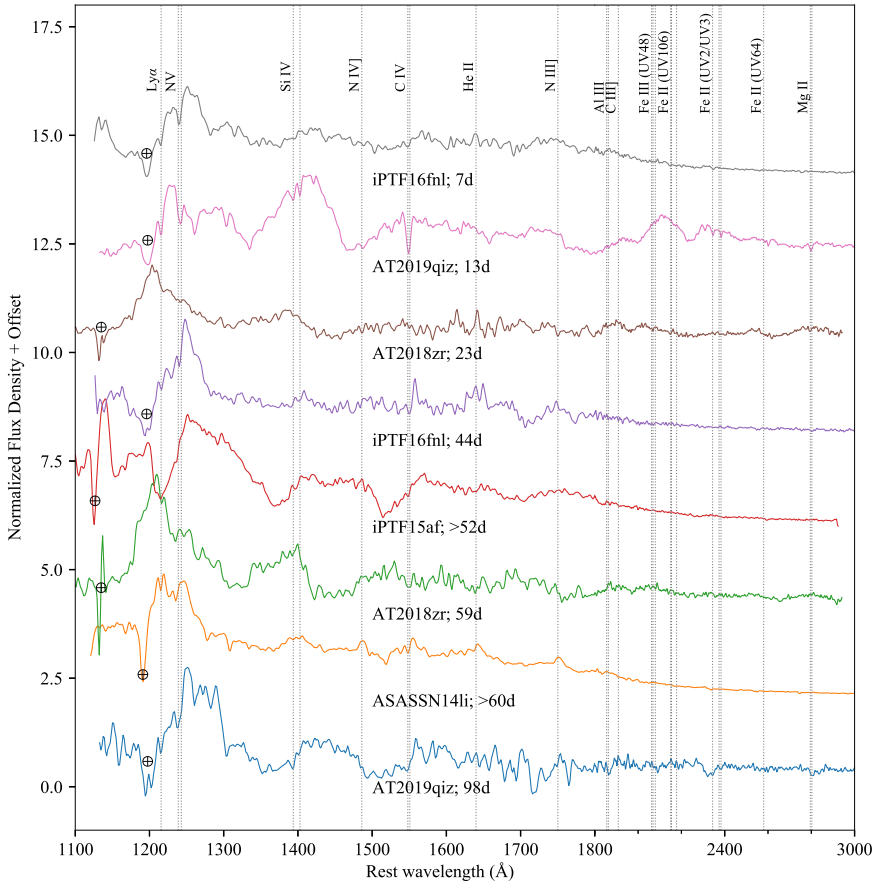

Figure 11. A compilation of TDE UV spectra normalized to rest wavelength 1700 Å. Most of the TDE UV spectra show fast-moving ($v \approx 10^3$–10^4 km s^{-1}) BAL features that signify the presence of outflows at some point of their evolution. The BAL features in TDEs are typically seen around high-ionization lines such as C IV $\lambda\lambda$1548, 1551 and Si IV λ1397 yet are usually absent from their NUV spectra. The $\Delta t = 13$ days spectrum of AT2019qiz is distinct from other known TDEs by having broad Fe features in the NUV. Note that the scale on the abscissa has been compressed for the NUV segment (1800–3000 Å) to allow more detailed examination of the FUV portion of the spectra.

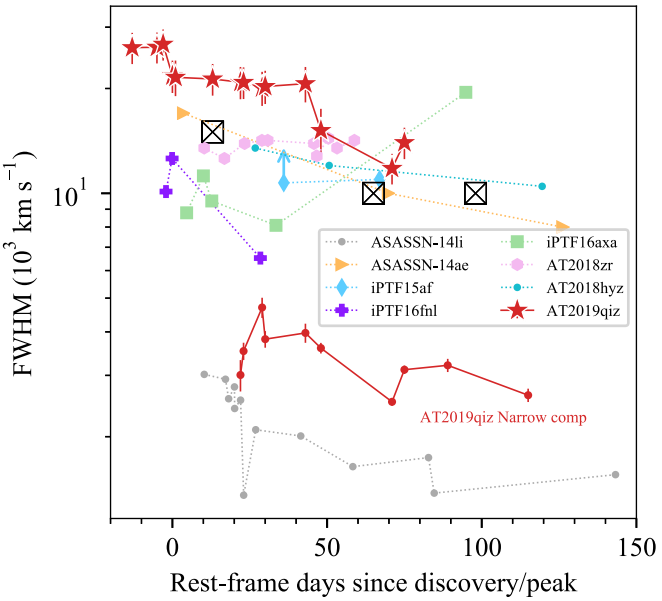

Figure 12. The evolution of the AT 2019qiz Hα FWHM compared with other TDEs. The FWHM of the broad Hα component is shown with red stars while the FWHM of the narrow Hα component is shown with red circles. Crossed boxes mark the BAL velocity at three HST epochs. It can be seen that the timing of the decrease in the broad Hα width is consistent with the change in outflow speed probed by the BALs.

wide-angle wind geometry in TDEs (Hung et al. 2019; Parkinson et al. 2020).

4.3. Origin of the Multicomponent Hα Emission

The accretion disk, outflow, and bound stellar debris are all possible production sites of Hα emission in a TDE. At a glance, the broad Hα component in AT 2019qiz may be reminiscent of a disk line profile with an intermediate inclination angle (i) such that the peaks corresponding to material moving away and toward the observer are not resolved (e.g., Liu et al. 2017; Holoien et al. 2019a). If due to rotation, the measured separation of ∼15,000 km s^{-1} between the two fitted peaks in the pre-peak epochs implies a disk size of $400\left(\frac{\sin i}{0.5}\right)^2 R_g$. However, the fast evolution of this broad component, with FWHM shrinking by as much as ∼50% in roughly 80 days, is hard to reconcile with the disk origin since changes in the disk geometry are expected to occur on longer timescales. In the double-peaked TDE AT 2018hyz, the Hα line widths remained roughly constant for at least 100 days (Figure 12; Hung et al. 2020).

The width of the broad Balmer emission in TDEs is typically of the order of 10^4 km s^{-1}. This value is comparable to the expected outflow velocity (e.g., Strubbe & Quataert 2009; Metzger & Stone 2016) in a TDE and therefore hints at the association. Roth & Kasen (2018) first proposed that

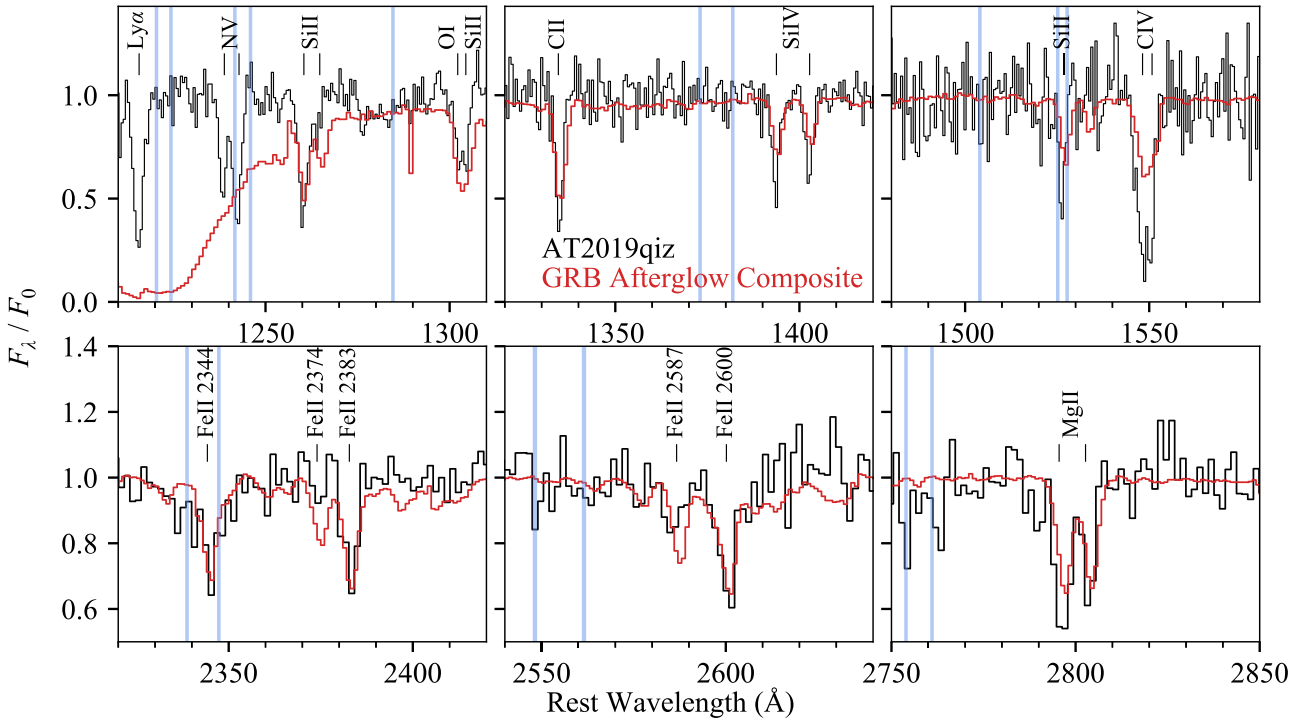

Figure 13. Comparison of the normalized spectrum of AT2019 qiz (black) with the GRB composite from Christensen et al. (2011) (red). We indicate the wavelength for different transitions in the host-galaxy rest frame with black labels and possible contamination by foreground absorption ($z \approx 0$) with blue vertical lines.

asymmetric emission lines may result from an optically thick, outflowing gas that is expected to be common in TDEs. The resulting line lacks the blueshifted absorption portion of a P Cygni line profile when the excitation temperature of the line is higher than the brightness temperature of the photosphere. Indeed, progressively more TDEs are found to have emission-line shapes deviating from a simple Gaussian (e.g., ASASSN-14ae, AT2018 zr, AT2018 hyz). Hung et al. (2019) found a good fit to the flat-topped Hα emission in AT2018 zr with this model, though an elliptical disk within a certain parameter space also produces such line shapes (Holoien et al. 2019a). N20 explored this possibility by comparing the model of Roth & Kasen (2018) with the spectra of AT 2019qiz. In summary, N20 found the model with an outflow velocity of 5000 km s^{-1} to be the best match to the Hα line profile at earlier and later epochs in AT 2019qiz. However, at the epochs where the Hα emission is the strongest, the model of Roth & Kasen (2018) fails to replicate the strong red wing of the line profile. The discrepancy may be resolved by adopting a higher opacity, changing the photosphere radius, or allowing for asymmetries in the outflow.

The potential correlation between the HST UV spectral features and the broad Hα component in AT 2019qiz could lend further support to the outflow origin of the broad Hα emission. We observed a reduction in the velocity of both the HiBALs in the UV and in the broad Hα component in the optical (Figure 12). The optical spectra with a higher cadence than the HST UV spectra find the FWHM to decrease from $\sim$22,000 km s^{-1} on $\Delta t = 13$ days to $\lesssim$15,000 km s^{-1} on $\Delta t \geqslant 48$ days. This change is well reflected in the $\Delta t = 65$ days HST spectra, which decelerated by $\sim$5000 km s^{-1} since the first HST observation on $\Delta t = 13$ days.

4.4. Origin of the Narrow UV Absorption Lines

As mentioned, we are unable to constrain the variability in the narrow absorption lines confidently owing to the lower S/N at the later HST epochs. However, the FUV spectrum from the second HST epoch does have sufficient S/N to reveal stronger absorption lines with $W_r \gtrsim 1.0$. We find these lines to have comparable strengths in the day 13 and day 65 spectra.

GRB afterglow spectra have long been exploited to study the intervening interstellar medium (ISM) and circumgalactic medium along the line of sight (e.g., Prochaska et al. 2007; Gatkine et al. 2019). To shine light on the origin of the narrow UV absorption lines in AT 2019qiz, we compare its spectrum with that of the GRB afterglow composite (Figure 13; Christensen et al. 2011). In AT 2019qiz, we derived $N(\mathrm{H\,I}) = 5 \times 10^{17}$ cm^{-2} from the CoG analysis. This column density is consistent with a Lyman-limit system, where the cloud starts to be dense enough to shield itself against the EUV background and remain neutral. GRB afterglow spectra, on the other hand, are often associated with a damped Lyα (DLA) system with a high neutral hydrogen column, $\log(N(\mathrm{H\,I})) > 20.3$ cm^{-2}. The DLA line is dominated by the Voigt profile, which is very different from the Gaussian-like Lyα line profile in AT 2019qiz (Figure 13).

We observe stronger Si IV and C IV absorption in AT 2019qiz than in the GRB composite. The strengths of the low-ionization species (Fe II and Mg II) are comparable to those in GRB afterglows. While the N V $\lambda\lambda$1238, 1242 absorption lines are well detected in AT 2019qiz, they are harder to identify in GRB spectra owing to blending with the red wing of Lyα. The high ionization potential of N^{4+} (77 eV) makes it difficult to produce in stellar radiation fields. Galactic halos and disks do have N V absorption, but none of them show a column

density $>10^{14.5}$ cm^{-2} (Prochaska et al. 2008, and references therein). Our measured N^{4+} column density of $\gtrsim 10^{15}$ cm^{-2} thus likely indicates a hard ionizing spectrum, which can be attributed to the TDE accretion disk or in part to the underlying weak AGN. The strong ionizing source may also explain the stronger Si IV and C IV W_r in AT 2019qiz than in the GRB composite. These high-ionization lines are likely to have formed in regions close to the SMBH rather than in the ISM. Our HST spectra cannot resolve fine-structure transitions such as Si II* and Fe II* in AT 2019qiz. In GRB afterglows, these fine-structure lines are thought to be produced by UV pumping and uniquely trace gas in the vicinity (100–1000 pc) of the burst (Prochaska 2006). We expect these lines to be detected in high-S/N, high-resolution TDE spectra since TDEs can also create a temporary UV radiation field.

Given that the redshift of the absorption lines is close to the host redshift, we consider both circumnuclear gas and the bound stellar debris as the candidate absorbing system. In ASASSN-14li, Cenko et al. (2016) also detected narrow absorption lines with a width of $\sim$500 km s^{-1}, comparable to that in AT 2019qiz. However, the absorption lines in ASASSN-14li are blueshifted by 250–400 km s^{-1} while the lines in AT 2019qiz do not appear to have a systemic velocity shift with respect to the host. The abundance pattern in ASASSN-14li is also very different. The low neutral hydrogen column of $\log(N(\mathrm{H\ I})) < 14.2$ cm^{-2} is somewhat expected in host galaxies with an old stellar population (Cenko et al. 2016). However, ASASSN-14li lacks the low-ionization Mg II $\lambda\lambda$2796, 2803 absorption that is commonly observed in cold ISM in the galaxy while having well-detected high-ionization lines. Together with the blueshift velocity being consistent with the outflow velocity measured from X-ray spectroscopy, Cenko et al. (2016) suggest that the low-velocity absorber is more likely the bound stellar debris on an elliptical orbit (Miller et al. 2015).

The absorber in AT 2019qiz has several properties different from those in ASASSN-14li. The low-ionization species, such as Fe II and Mg II, are readily detected in AT 2019qiz with W_r comparable to those observed in GRB afterglow and QSO spectra, where the absorbing systems have been associated with galaxies. The likely lack of variability also counters the scenario in which the absorbing gas is the bound stellar debris. Clumpiness or bulk motion of the debris stream could easily alter the gas density and therefore lead to variability in the absorption lines on the fallback timescale $t_{\mathrm{fallback}} \approx 40$ days. Therefore, we conclude that the absorption lines in AT2019 qiz are more likely to be probing the host ISM and circumnuclear gas instead of the stellar debris as in ASASSN-14li.

5. Conclusions

The early classification of AT 2019qiz and its proximity allow us to perform a detailed, multiwavelength study of a TDE. Our UV and optical follow-up observations in both photometric and spectroscopic modes offer new insights for optically selected TDEs. AT 2019qiz is located in a galaxy with a weak AGN, as evidenced by the line ratios in the BPT diagram. The evolution timescale and luminosity of AT 2019qiz are fast and faint, making it an intermediate event between iPTF16fnl and the rest of the TDE population.

Both the photosphere evolution and the BALs in the HST spectra strongly corroborate the outflow scenario in TDEs. We find the photosphere to be expanding at a constant velocity $v \approx 2700$ km s^{-1} before reaching t_{peak}. The early luminosity evolution in AT 2019qiz follows a power law ($\propto t^2$), consistent with the prediction of an expanding fireball. The BALs are detected at all three HST epochs with a decrease in outflow velocity from 15,000 to 10,000 km s^{-1}. This deceleration is expected as the mass fallback rate declines at later times.

The UV spectrum at the first HST epoch is unlike that of all the TDEs observed in the past, because it contains both HiBAL and FeLoBAL features such as Al III and Fe II. The UV spectrum of AT 2019qiz resembles that of the SLSN Gaia16apd at maximum light more than that of any known FeLoBAL QSO. However, the broad Mg II $\lambda\lambda$2796, 2803 doublet, which is readily found in both Gaia16apd and FeLoBAL QSOs, is not detected in AT 2019qiz. The disappearance of the FeLoBAL features at the two later HST epochs of AT 2019qiz is likely due to the thinning of the X-ray/EUV shielding material as the mass fallback/accretion rate decreases with time.

The detection of He II λ4686 and the Balmer emission since the beginning of the monitoring up to day 89 makes AT 2019qiz a TDE-Bowen in the spectral classification scheme proposed by van Velzen et al. (2020). We carefully studied the Hα emission and found the line profile to be characterized by a very broad component with FWHM $\gtrsim 10^4$ km s^{-1} and a narrower component with FWHM ≈ 3000 km s^{-1} that only appeared after $\Delta t \gtrsim 22$ days. The broad Hα component narrows with time as observed in other TDEs and becomes progressively more symmetric around the rest wavelength of Hα. We inferred that the broad Hα evolution is most likely to be driven by the outflow given the similar value of the Hα line width and the BAL velocity, and the fact that the timing of the decrease in broad Hα width is seen to be coincident with the decrease in wind velocity probed by the BALs.

We also analyzed the narrow absorption lines in the first HST spectrum and derived ionic column densities for several species using the CoG method. The measured Lyα W_r corresponds to a Lyman-limit system, where the high-ionization species have stronger W_r and the low-ionization lines have similar W_r to those in GRB afterglows. We concluded that the narrow absorption lines are more likely to be probing the gas in the host galaxy rather than the bound stellar debris as in the case of ASASSN-14li. The UV spectra of AT 2019qiz demonstrate the potential of using TDEs to probe circumnuclear gas and the ISM in TDE host galaxies. Future high-S/N and high-resolution UV spectra will allow us to resolve the fine-structure lines produced by UV pumping in TDEs and study the gas in the vicinity of the SMBHs.

We thank anonymous referee for helpful suggestions that greatly improved the quality of the paper. T.H. is grateful to Ari Laor, Alexei Baskin, and Frederick Hamann for generously sharing their insightful thoughts on the UV spectral signatures in AT 2019qiz and providing BALQSO templates for comparison. She also thanks Dan Perley for helpful discussion on the similarities between AT 2019qiz and Gaia16apd. T.H. thanks Elizabeth Nance and John Debes for their help with scheduling the HST ToO observations.

The UCSC transient team is supported in part by National Science Foundation (NSF) grant AST-1518052, National Aeronautics and Space Administration (NASA) Swift grant 80NSSC19K1386, the Gordon & Betty Moore Foundation, the Heising-Simons Foundation, and by a fellowship to R.J.F. from

the David and Lucile Packard Foundation. K.A.A., E.R.-R., and B.M. are supported by the Danish National Research Foundation (DNRF132), the Heising-Simons Foundation, and NSF grant AST-161588. J.L.D. is supported by the GRF grant from the Hong Kong government under HKU 27305119. M.R.S. is supported by the NSF Graduate Research Fellowship Program Under grant 1842400. A.V.F.'s group is grateful for generous financial assistance from the Christopher R. Redlich Fund, the TABASGO Foundation, and the Miller Institute for Basic Research in Science (U.C. Berkeley; A.V.F. is a Miller Senior Fellow). Support for T.W.-S.H. was provided by NASA through NASA Hubble Fellowship grant HST-HF2-51458.001-A awarded by the Space Telescope Science Institute (STScI), which is operated by the Association of Universities for Research in Astronomy (AURA), Inc., under NASA contract NAS 5-26555. Parts of this research were supported by the Australian Research Council Centre of Excellence for All Sky Astrophysics in 3 Dimensions (ASTRO 3D), through project number CE170100013. Research at Lick Observatory is partially supported by a generous gift from Google.

This work is based on observations made with the NASA/ESA Hubble Space Telescope under program number GO-16026. Support for program GO-16026 was provided by NASA through a grant from STScI, which is operated by AURA, Inc., under NASA contract NAS 5-26555. This work makes use of observations from the Las Cumbres Observatory global telescope network following the approved program 2019B-0363. Some of the data presented herein were obtained at the W. M. Keck Observatory, which is operated as a scientific partnership among the California Institute of Technology, the University of California, and NASA. The Observatory was made possible by the generous financial support of the W. M. Keck Foundation. The authors wish to recognize and acknowledge the very significant cultural role and reverence that the summit of Maunakea has always had within the indigenous Hawaiian community. We are most fortunate to have the opportunity to conduct observations from this mountain.

Based in part on observations obtained at the Southern Astrophysical Research (SOAR) telescope, which is a joint project of the Ministério da Ciência, Tecnologia, Inovações e Comunicações (MCTIC) do Brasil, the U.S. National Optical Astronomy Observatory (NOAO), the University of North Carolina at Chapel Hill (UNC), and Michigan State University (MSU). This work includes data obtained with the Swope Telescope at Las Campanas Observatory, Chile, as part of the Swope Time Domain Key Project (PI Piro, Co-Is Burns, Cowperthwaite, Dimitriadis, Drout, Foley, French, Holoien, Hsiao, Kilpatrick, Madore, Phillips, and Rojas-Bravo). The authors thank Swope Telescope observers Jorge Anais Vilchez, Abdo Campillay, Yilin Kong Riveros, and Natalie Ulloa for collecting data presented in this paper.

Software: photpipe imaging and photometry pipeline (Rest et al. 2005, 2014), hotpants (Becker 2015), DoPhot (Schechter et al. 1993), PyRAF (Science Software Branch at STScI 2012), pPXF (Cappellari 2017), Prospector (Leja et al. 2017), HEASoft (NASA High Energy Astrophysics Science Archive Research Center (Heasarc), 2014), MOSFiT (Guillochon et al. 2018; Mockler et al. 2019).

Appendix

We present the reduced UV and optical photometric data that are analyzed in this paper in Table A1. The observing details can be found in Sections 2.2 and 2.3. Milky Way extinction has been corrected for all the data.

Table A1
Photometric Data of AT 2019qiz

MJD	Magnitude	Filter	Telescope
58753.059	16.10 ± 0.04	*UVW2*	Swift
58755.388	16.01 ± 0.05	*UVW2*	Swift
58756.436	15.79 ± 0.05	*UVW2*	Swift
58763.212	15.16 ± 0.05	*UVW2*	Swift
58766.074	15.34 ± 0.04	*UVW2*	Swift
58769.324	15.60 ± 0.04	*UVW2*	Swift
58772.787	15.82 ± 0.11	*UVW2*	Swift
58778.548	16.27 ± 0.05	*UVW2*	Swift
58781.681	16.85 ± 0.06	*UVW2*	Swift
58784.603	16.61 ± 0.05	*UVW2*	Swift
58787.063	16.83 ± 0.06	*UVW2*	Swift
58790.640	16.99 ± 0.06	*UVW2*	Swift
58796.034	17.10 ± 0.13	*UVW2*	Swift
58799.813	17.14 ± 0.07	*UVW2*	Swift
58802.925	17.24 ± 0.07	*UVW2*	Swift
58805.257	17.41 ± 0.08	*UVW2*	Swift
58809.101	17.50 ± 0.07	*UVW2*	Swift
58815.346	17.58 ± 0.07	*UVW2*	Swift
58820.980	17.99 ± 0.09	*UVW2*	Swift
58825.841	18.01 ± 0.09	*UVW2*	Swift
58836.845	18.47 ± 0.14	*UVW2*	Swift
58847.951	18.59 ± 0.11	*UVW2*	Swift
58852.583	18.60 ± 0.11	*UVW2*	Swift
58857.113	18.88 ± 0.13	*UVW2*	Swift
58862.350	18.92 ± 0.13	*UVW2*	Swift
58867.939	19.09 ± 0.19	*UVW2*	Swift
58929.624	19.38 ± 0.18	*UVW2*	Swift
58753.064	16.17 ± 0.05	*UVM2*	Swift
58755.392	16.05 ± 0.05	*UVM2*	Swift
58756.439	15.79 ± 0.05	*UVM2*	Swift
58763.214	15.08 ± 0.05	*UVM2*	Swift
58766.078	15.08 ± 0.04	*UVM2*	Swift
58769.328	15.26 ± 0.04	*UVM2*	Swift
58778.551	15.89 ± 0.05	*UVM2*	Swift
58781.684	16.31 ± 0.05	*UVM2*	Swift
58784.606	16.24 ± 0.05	*UVM2*	Swift
58787.066	16.39 ± 0.05	*UVM2*	Swift
58790.643	16.57 ± 0.05	*UVM2*	Swift
58799.816	16.82 ± 0.06	*UVM2*	Swift
58802.928	16.88 ± 0.06	*UVM2*	Swift
58805.259	17.02 ± 0.07	*UVM2*	Swift
58809.104	17.26 ± 0.07	*UVM2*	Swift
58815.349	17.52 ± 0.07	*UVM2*	Swift
58820.983	17.62 ± 0.08	*UVM2*	Swift
58825.844	17.96 ± 0.09	*UVM2*	Swift
58836.847	18.07 ± 0.11	*UVM2*	Swift
58847.955	18.39 ± 0.10	*UVM2*	Swift
58852.587	18.57 ± 0.10	*UVM2*	Swift
58857.117	18.61 ± 0.11	*UVM2*	Swift
58862.353	18.69 ± 0.11	*UVM2*	Swift
58867.941	18.98 ± 0.18	*UVM2*	Swift
58910.346	18.95 ± 0.09	*UVM2*	Swift
58934.139	19.68 ± 0.30	*UVM2*	Swift
58753.054	16.31 ± 0.05	*UVW1*	Swift
58755.385	16.16 ± 0.05	*UVW1*	Swift

Table A1
(Continued)

MJD	Magnitude	Filter	Telescope
58756.433	15.97 ± 0.05	*UVW*1	Swift
58759.755	15.53 ± 0.05	*UVW*1	Swift
58759.768	15.47 ± 0.05	*UVW*1	Swift
58760.637	15.44 ± 0.05	*UVW*1	Swift
58763.211	15.30 ± 0.05	*UVW*1	Swift
58766.071	15.31 ± 0.05	*UVW*1	Swift
58769.321	15.43 ± 0.05	*UVW*1	Swift
58771.188	15.56 ± 0.04	*UVW*1	Swift
58771.201	15.55 ± 0.04	*UVW*1	Swift
58772.784	15.63 ± 0.05	*UVW*1	Swift
58778.545	15.97 ± 0.05	*UVW*1	Swift
58781.678	16.24 ± 0.06	*UVW*1	Swift
58784.600	16.28 ± 0.06	*UVW*1	Swift
58787.060	16.46 ± 0.06	*UVW*1	Swift
58790.637	16.57 ± 0.06	*UVW*1	Swift
58796.030	16.72 ± 0.06	*UVW*1	Swift
58799.810	16.83 ± 0.07	*UVW*1	Swift
58802.922	16.99 ± 0.07	*UVW*1	Swift
58805.255	17.21 ± 0.09	*UVW*1	Swift
58809.098	17.24 ± 0.08	*UVW*1	Swift
58815.343	17.40 ± 0.08	*UVW*1	Swift
58820.977	17.63 ± 0.09	*UVW*1	Swift
58825.838	17.60 ± 0.09	*UVW*1	Swift
58836.844	18.02 ± 0.13	*UVW*1	Swift
58847.949	18.13 ± 0.11	*UVW*1	Swift
58852.580	18.21 ± 0.11	*UVW*1	Swift
58857.110	18.46 ± 0.13	*UVW*1	Swift
58862.347	18.44 ± 0.12	*UVW*1	Swift
58867.278	18.68 ± 0.14	*UVW*1	Swift
58899.463	18.70 ± 0.10	*UVW*1	Swift
58919.532	18.89 ± 0.14	*UVW*1	Swift
58751.989	15.98 ± 0.17	*u*	Siding Spring 1 m
58752.350	16.38 ± 0.17	*u*	Swope
58753.268	16.38 ± 0.17	*u*	Swope
58754.335	16.23 ± 0.17	*u*	Swope
58754.759	15.98 ± 0.17	*u*	Siding Spring 1 m
58755.381	15.91 ± 0.17	*u*	Swope
58757.979	15.48 ± 0.17	*u*	Siding Spring 1 m
58759.328	15.56 ± 0.17	*u*	Swope
58760.366	15.43 ± 0.17	*u*	Swope
58760.965	15.35 ± 0.17	*u*	Siding Spring 1 m
58761.336	15.34 ± 0.17	*u*	Swope
58762.262	15.36 ± 0.17	*u*	Swope
58763.961	15.24 ± 0.17	*u*	Siding Spring 1 m
58766.592	15.20 ± 0.17	*u*	Siding Spring 1 m
58769.655	15.32 ± 0.17	*u*	Siding Spring 1 m
58772.596	15.40 ± 0.17	*u*	Siding Spring 1 m
58774.316	15.59 ± 0.17	*u*	Swope
58775.275	15.61 ± 0.17	*u*	Swope
58776.322	15.82 ± 0.17	*u*	Swope
58777.324	15.76 ± 0.17	*u*	Swope
58778.242	15.82 ± 0.17	*u*	Swope
58778.649	15.63 ± 0.17	*u*	Siding Spring 1 m
58781.729	15.71 ± 0.17	*u*	Siding Spring 1 m
58783.318	16.09 ± 0.17	*u*	Swope
58784.269	16.09 ± 0.17	*u*	Swope
58784.740	15.96 ± 0.17	*u*	Siding Spring 1 m
58785.287	16.21 ± 0.17	*u*	Swope
58786.300	16.17 ± 0.17	*u*	Swope
58787.249	16.31 ± 0.17	*u*	Swope
58787.580	15.90 ± 0.18	*u*	Siding Spring 1 m
58787.587	16.62 ± 0.18	*u*	Siding Spring 1 m
58789.157	16.39 ± 0.17	*u*	Swope

Table A1
(Continued)

MJD	Magnitude	Filter	Telescope
58790.943	16.09 ± 0.17	*u*	Siding Spring 1 m
58791.317	16.39 ± 0.17	*u*	Swope
58793.521	15.95 ± 0.17	*u*	Siding Spring 1 m
58796.628	16.20 ± 0.17	*u*	Siding Spring 1 m
58802.499	16.75 ± 0.17	*u*	Siding Spring 1 m
58805.312	16.96 ± 0.17	*u*	Swope
58805.571	16.43 ± 0.17	*u*	Siding Spring 1 m
58806.299	17.03 ± 0.17	*u*	Swope
58807.301	16.97 ± 0.17	*u*	Swope
58808.297	17.13 ± 0.17	*u*	Swope
58808.589	16.67 ± 0.17	*u*	Siding Spring 1 m
58811.825	16.80 ± 0.17	*u*	Siding Spring 1 m
58813.183	17.16 ± 0.17	*u*	Swope
58814.292	17.35 ± 0.17	*u*	Swope
58814.634	16.99 ± 0.17	*u*	Siding Spring 1 m
58815.297	17.31 ± 0.17	*u*	Swope
58817.241	17.33 ± 0.17	*u*	Swope
58834.126	18.14 ± 0.17	*u*	Swope
58835.257	18.19 ± 0.17	*u*	Swope
58836.203	17.64 ± 0.17	*u*	Swope
58839.207	17.95 ± 0.17	*u*	Swope
58840.219	18.10 ± 0.17	*u*	Swope
58849.225	18.57 ± 0.17	*u*	Swope
58851.111	18.51 ± 0.17	*u*	Swope
58853.088	18.69 ± 0.17	*u*	Swope
58869.057	18.25 ± 0.17	*u*	Swope
58871.096	19.27 ± 0.17	*u*	Swope
58873.186	18.86 ± 0.17	*u*	Swope
58882.185	19.18 ± 0.17	*u*	Swope
58885.168	20.02 ± 0.17	*u*	Swope
58893.082	19.45 ± 0.17	*u*	Swope
58904.080	19.37 ± 0.17	*u*	Swope
58909.081	20.77 ± 0.17	*u*	Swope
58716.503	>18.97	*g*	Palomar 48 in
58719.501	>19.17	*g*	Palomar 48 in
58722.463	>19.95	*g*	Palomar 48 in
58725.479	>20.06	*g*	Palomar 48 in
58732.437	>20.00	*g*	Palomar 48 in
58735.444	>20.01	*g*	Palomar 48 in
58739.501	>19.17	*g*	Palomar 48 in
58742.504	>18.86	*g*	Palomar 48 in
58746.504	17.28 ± 0.05	*g*	Palomar 48 in
58748.521	16.90 ± 0.05	*g*	Palomar 48 in
58749.470	16.77 ± 0.04	*g*	Palomar 48 in
58751.495	16.57 ± 0.04	*g*	Palomar 48 in
58751.785	16.50 ± 0.01	*g*	Siding Spring 1 m
58752.348	16.52 ± 0.01	*g*	Swope
58753.266	16.42 ± 0.01	*g*	Swope
58754.331	16.38 ± 0.01	*g*	Swope
58755.379	16.22 ± 0.01	*g*	Swope
58756.423	16.11 ± 0.03	*g*	Palomar 48 in
58757.389	15.95 ± 0.04	*g*	Palomar 48 in
58757.946	15.84 ± 0.01	*g*	Siding Spring 1 m
58759.327	15.70 ± 0.01	*g*	Swope
58759.439	15.70 ± 0.04	*g*	Palomar 48 in
58760.364	15.57 ± 0.01	*g*	Swope
58760.936	15.49 ± 0.01	*g*	Siding Spring 1 m
58761.331	15.61 ± 0.01	*g*	Swope
58762.261	15.50 ± 0.01	*g*	Swope
58763.459	15.44 ± 0.02	*g*	Palomar 48 in
58763.931	15.36 ± 0.01	*g*	Siding Spring 1 m
58766.408	15.49 ± 0.03	*g*	Palomar 48 in
58766.771	15.49 ± 0.01	*g*	Siding Spring 1 m

Table A1
(Continued)

MJD	Magnitude	Filter	Telescope
58769.556	15.62 ± 0.02	*g*	Siding Spring 1 m
58772.336	15.67 ± 0.04	*g*	Palomar 48 in
58772.552	15.79 ± 0.02	*g*	Siding Spring 1 m
58772.565	15.75 ± 0.02	*g*	Siding Spring 1 m
58774.315	15.77 ± 0.01	*g*	Swope
58775.274	15.80 ± 0.01	*g*	Swope
58775.438	15.80 ± 0.04	*g*	Palomar 48 in
58776.321	15.82 ± 0.01	*g*	Swope
58777.323	15.92 ± 0.01	*g*	Swope
58778.241	16.01 ± 0.01	*g*	Swope
58778.312	15.92 ± 0.04	*g*	Palomar 48 in
58778.580	15.92 ± 0.01	*g*	Siding Spring 1 m
58781.414	16.10 ± 0.04	*g*	Palomar 48 in
58781.732	16.08 ± 0.01	*g*	Siding Spring 1 m
58783.316	16.11 ± 0.01	*g*	Swope
58784.267	16.27 ± 0.01	*g*	Swope
58784.727	16.24 ± 0.01	*g*	Siding Spring 1 m
58785.284	16.25 ± 0.01	*g*	Swope
58786.298	16.28 ± 0.01	*g*	Swope
58787.247	16.31 ± 0.01	*g*	Swope
58787.433	16.38 ± 0.05	*g*	Palomar 48 in
58787.689	16.36 ± 0.01	*g*	Siding Spring 1 m
58789.155	16.41 ± 0.01	*g*	Swope
58790.335	16.49 ± 0.04	*g*	Palomar 48 in
58790.941	16.38 ± 0.01	*g*	Siding Spring 1 m
58791.316	16.53 ± 0.01	*g*	Swope
58793.350	16.61 ± 0.04	*g*	Palomar 48 in
58793.504	16.63 ± 0.01	*g*	Siding Spring 1 m
58796.632	16.69 ± 0.01	*g*	Siding Spring 1 m
58799.833	16.89 ± 0.04	*g*	Siding Spring 1 m
58800.236	16.86 ± 0.07	*g*	Palomar 48 in
58802.508	16.97 ± 0.02	*g*	Siding Spring 1 m
58803.226	16.92 ± 0.14	*g*	Palomar 48 in
58804.295	17.15 ± 0.01	*g*	Swope
58805.310	17.12 ± 0.01	*g*	Swope
58805.518	17.04 ± 0.02	*g*	Siding Spring 1 m
58806.297	17.12 ± 0.01	*g*	Swope
58806.372	17.10 ± 0.06	*g*	Palomar 48 in
58807.300	17.19 ± 0.01	*g*	Swope
58808.296	17.16 ± 0.01	*g*	Swope
58808.566	17.11 ± 0.02	*g*	Siding Spring 1 m
58811.817	17.22 ± 0.02	*g*	Siding Spring 1 m
58812.333	17.34 ± 0.05	*g*	Palomar 48 in
58813.182	17.32 ± 0.01	*g*	Swope
58814.291	17.43 ± 0.01	*g*	Swope
58814.524	17.39 ± 0.02	*g*	Siding Spring 1 m
58815.296	17.39 ± 0.01	*g*	Swope
58817.240	17.53 ± 0.01	*g*	Swope
58820.230	17.56 ± 0.13	*g*	Palomar 48 in
58829.239	17.98 ± 0.03	*g*	Swope
58830.180	17.99 ± 0.02	*g*	Swope
58831.187	17.98 ± 0.03	*g*	Swope
58833.208	17.88 ± 0.10	*g*	Palomar 48 in
58834.122	18.00 ± 0.01	*g*	Swope
58835.254	18.08 ± 0.01	*g*	Swope
58836.202	18.15 ± 0.01	*g*	Swope
58839.205	18.26 ± 0.01	*g*	Swope
58840.217	18.24 ± 0.01	*g*	Swope
58849.221	18.56 ± 0.01	*g*	Swope
58851.106	18.52 ± 0.01	*g*	Swope
58853.083	18.51 ± 0.02	*g*	Swope
58863.148	19.07 ± 0.14	*g*	Palomar 48 in
58867.188	18.83 ± 0.12	*g*	Palomar 48 in
58869.054	18.87 ± 0.02	*g*	Swope

Table A1
(Continued)

MJD	Magnitude	Filter	Telescope
58871.088	18.89 ± 0.02	*g*	Swope
58872.194	19.02 ± 0.15	*g*	Palomar 48 in
58873.127	18.95 ± 0.10	*g*	Palomar 48 in
58873.182	18.97 ± 0.01	*g*	Swope
58874.188	19.12 ± 0.17	*g*	Palomar 48 in
58875.166	19.09 ± 0.11	*g*	Palomar 48 in
58876.147	19.04 ± 0.01	*g*	Swope
58876.169	19.01 ± 0.12	*g*	Palomar 48 in
58876.169	19.01 ± 0.11	*g*	Palomar 48 in
58877.169	19.16 ± 0.17	*g*	Palomar 48 in
58877.178	19.09 ± 0.02	*g*	Swope
58878.213	19.14 ± 0.26	*g*	Palomar 48 in
58880.126	19.10 ± 0.16	*g*	Palomar 48 in
58881.147	19.18 ± 0.20	*g*	Palomar 48 in
58881.148	19.03 ± 0.17	*g*	Palomar 48 in
58882.179	19.11 ± 0.03	*g*	Swope
58885.125	19.08 ± 0.22	*g*	Palomar 48 in
58885.164	19.37 ± 0.09	*g*	Swope
58891.186	19.32 ± 0.18	*g*	Palomar 48 in
58893.078	19.32 ± 0.01	*g*	Swope
58893.168	19.53 ± 0.17	*g*	Palomar 48 in
58894.171	19.24 ± 0.14	*g*	Palomar 48 in
58894.172	19.33 ± 0.19	*g*	Palomar 48 in
58895.144	19.33 ± 0.19	*g*	Palomar 48 in
58896.148	19.43 ± 0.14	*g*	Swope
58897.120	19.37 ± 0.02	*g*	Swope
58898.171	19.46 ± 0.20	*g*	Palomar 48 in
58898.179	19.56 ± 0.20	*g*	Palomar 48 in
58899.149	19.58 ± 0.16	*g*	Palomar 48 in
58904.075	19.53 ± 0.02	*g*	Swope
58904.133	19.65 ± 0.20	*g*	Palomar 48 in
58909.076	19.49 ± 0.02	*g*	Swope
58911.110	19.61 ± 0.04	*g*	Swope
58921.073	19.71 ± 0.04	*g*	Swope
58716.481	>19.30	*r*	Palomar 48 in
58719.477	>19.16	*r*	Palomar 48 in
58722.500	>20.20	*r*	Palomar 48 in
58725.497	>20.26	*r*	Palomar 48 in
58730.479	>19.86	*r*	Palomar 48 in
58735.487	>20.10	*r*	Palomar 48 in
58739.462	>19.42	*r*	Palomar 48 in
58745.500	>19.10	*r*	Palomar 48 in
58745.500	17.57 ± 0.07	*r*	Palomar 48 in
58748.481	17.18 ± 0.05	*r*	Palomar 48 in
58751.502	16.75 ± 0.04	*r*	Palomar 48 in
58751.783	16.74 ± 0.01	*r*	Siding Spring 1 m
58752.344	16.67 ± 0.01	*r*	Swope
58753.261	16.62 ± 0.01	*r*	Swope
58754.327	16.56 ± 0.01	*r*	Swope
58754.762	16.49 ± 0.01	*r*	Siding Spring 1 m
58755.376	16.36 ± 0.01	*r*	Swope
58757.474	16.10 ± 0.04	*r*	Palomar 48 in
58757.944	16.07 ± 0.01	*r*	Siding Spring 1 m
58759.323	15.87 ± 0.01	*r*	Swope
58760.361	15.76 ± 0.00	*r*	Swope
58760.947	15.76 ± 0.01	*r*	Siding Spring 1 m
58761.328	15.70 ± 0.00	*r*	Swope
58762.259	15.65 ± 0.00	*r*	Swope
58763.499	15.57 ± 0.03	*r*	Palomar 48 in
58763.928	15.59 ± 0.01	*r*	Siding Spring 1 m
58763.945	15.57 ± 0.01	*r*	Siding Spring 1 m
58766.482	15.58 ± 0.03	*r*	Palomar 48 in
58766.603	15.70 ± 0.13	*r*	Siding Spring 1 m
58766.767	15.65 ± 0.01	*r*	Siding Spring 1 m

Table A1
(Continued)

MJD	Magnitude	Filter	Telescope
58769.431	15.67 ± 0.04	*r*	Palomar 48 in
58769.559	15.75 ± 0.03	*r*	Siding Spring 1 m
58772.379	15.78 ± 0.03	*r*	Palomar 48 in
58772.548	15.89 ± 0.03	*r*	Siding Spring 1 m
58774.312	15.83 ± 0.01	*r*	Swope
58775.357	15.81 ± 0.03	*r*	Palomar 48 in
58776.318	15.89 ± 0.01	*r*	Swope
58777.321	15.92 ± 0.01	*r*	Swope
58778.239	16.17 ± 0.01	*r*	Swope
58778.458	15.91 ± 0.03	*r*	Palomar 48 in
58778.574	16.00 ± 0.01	*r*	Siding Spring 1 m
58781.958	16.11 ± 0.01	*r*	Siding Spring 1 m
58783.312	16.12 ± 0.01	*r*	Swope
58784.264	16.24 ± 0.00	*r*	Swope
58784.392	16.18 ± 0.05	*r*	Palomar 48 in
58784.729	16.26 ± 0.01	*r*	Siding Spring 1 m
58785.283	16.23 ± 0.01	*r*	Swope
58786.295	16.30 ± 0.01	*r*	Swope
58787.244	16.33 ± 0.01	*r*	Swope
58787.583	16.38 ± 0.02	*r*	Siding Spring 1 m
58789.152	16.40 ± 0.01	*r*	Swope
58790.369	16.44 ± 0.04	*r*	Palomar 48 in
58790.938	16.47 ± 0.01	*r*	Siding Spring 1 m
58791.314	16.49 ± 0.01	*r*	Swope
58793.472	16.58 ± 0.04	*r*	Palomar 48 in
58793.506	16.60 ± 0.01	*r*	Siding Spring 1 m
58796.319	16.69 ± 0.05	*r*	Palomar 48 in
58796.625	16.70 ± 0.01	*r*	Siding Spring 1 m
58799.837	16.72 ± 0.03	*r*	Siding Spring 1 m
58802.505	16.91 ± 0.02	*r*	Siding Spring 1 m
58803.314	16.94 ± 0.04	*r*	Palomar 48 in
58804.293	16.92 ± 0.01	*r*	Swope
58805.308	16.96 ± 0.01	*r*	Swope
58805.516	17.04 ± 0.02	*r*	Siding Spring 1 m
58806.294	17.06 ± 0.01	*r*	Swope
58806.317	17.06 ± 0.05	*r*	Palomar 48 in
58807.297	17.05 ± 0.01	*r*	Swope
58808.294	17.17 ± 0.01	*r*	Swope
58808.593	17.08 ± 0.03	*r*	Siding Spring 1 m
58811.815	17.19 ± 0.01	*r*	Siding Spring 1 m
58812.274	17.28 ± 0.06	*r*	Palomar 48 in
58813.179	17.24 ± 0.01	*r*	Swope
58814.288	17.35 ± 0.01	*r*	Swope
58814.549	17.38 ± 0.02	*r*	Siding Spring 1 m
58815.293	17.32 ± 0.01	*r*	Swope
58817.238	17.48 ± 0.01	*r*	Swope
58827.194	17.96 ± 0.02	*r*	Swope
58828.207	18.03 ± 0.02	*r*	Swope
58829.234	17.84 ± 0.03	*r*	Swope
58830.175	18.20 ± 0.02	*r*	Swope
58830.251	17.80 ± 0.09	*r*	Palomar 48 in
58831.183	17.83 ± 0.02	*r*	Swope
58833.251	17.99 ± 0.07	*r*	Palomar 48 in
58833.325	17.99 ± 0.09	*r*	Palomar 48 in
58834.116	17.90 ± 0.01	*r*	Swope
58835.250	17.89 ± 0.01	*r*	Swope
58836.198	17.93 ± 0.01	*r*	Swope
58837.237	18.00 ± 0.06	*r*	Palomar 48 in
58839.201	18.10 ± 0.01	*r*	Swope
58840.213	18.10 ± 0.01	*r*	Swope
58849.215	18.39 ± 0.01	*r*	Swope
58851.098	18.39 ± 0.01	*r*	Swope
58853.074	18.45 ± 0.02	*r*	Swope

Table A1
(Continued)

MJD	Magnitude	Filter	Telescope
58854.169	18.45 ± 0.21	*r*	Palomar 48 in
58860.168	18.50 ± 0.10	*r*	Palomar 48 in
58860.208	18.55 ± 0.18	*r*	Palomar 48 in
58861.214	18.68 ± 0.15	*r*	Palomar 48 in
58867.231	18.75 ± 0.11	*r*	Palomar 48 in
58869.047	18.67 ± 0.02	*r*	Swope
58871.084	18.78 ± 0.03	*r*	Swope
58872.260	18.78 ± 0.14	*r*	Palomar 48 in
58873.161	18.94 ± 0.12	*r*	Palomar 48 in
58873.174	18.85 ± 0.02	*r*	Swope
58875.196	18.99 ± 0.12	*r*	Palomar 48 in
58876.139	18.96 ± 0.01	*r*	Swope
58877.146	19.08 ± 0.12	*r*	Palomar 48 in
58877.170	18.92 ± 0.02	*r*	Swope
58878.170	18.94 ± 0.26	*r*	Palomar 48 in
58878.171	18.38 ± 0.17	*r*	Palomar 48 in
58881.107	18.92 ± 0.15	*r*	Palomar 48 in
58881.108	18.95 ± 0.16	*r*	Palomar 48 in
58882.169	19.82 ± 0.26	*r*	Swope
58882.170	18.80 ± 0.02	*r*	Swope
58885.155	18.95 ± 0.06	*r*	Swope
58886.130	18.86 ± 0.17	*r*	Palomar 48 in
58887.126	18.90 ± 0.21	*r*	Palomar 48 in
58891.129	19.39 ± 0.19	*r*	Palomar 48 in
58893.069	19.77 ± 0.10	*r*	Swope
58893.070	19.08 ± 0.02	*r*	Swope
58894.144	19.26 ± 0.12	*r*	Palomar 48 in
58895.108	19.22 ± 0.12	*r*	Palomar 48 in
58896.122	19.15 ± 0.05	*r*	Swope
58896.125	19.26 ± 0.04	*r*	Swope
58897.109	19.30 ± 0.09	*r*	Swope
58897.110	19.03 ± 0.02	*r*	Swope
58898.129	19.27 ± 0.14	*r*	Palomar 48 in
58904.065	19.82 ± 0.13	*r*	Swope
58904.066	19.25 ± 0.02	*r*	Swope
58909.065	19.23 ± 0.02	*r*	Swope
58911.099	19.45 ± 0.03	*r*	Swope
58921.062	19.34 ± 0.03	*r*	Swope
58752.346	16.86 ± 0.01	*i*	Swope
58753.264	16.79 ± 0.01	*i*	Swope
58754.329	16.67 ± 0.01	*i*	Swope
58755.378	16.66 ± 0.01	*i*	Swope
58759.325	16.07 ± 0.01	*i*	Swope
58760.363	15.92 ± 0.01	*i*	Swope
58761.330	15.88 ± 0.00	*i*	Swope
58762.260	15.84 ± 0.01	*i*	Swope
58774.314	15.95 ± 0.01	*i*	Swope
58776.320	16.01 ± 0.01	*i*	Swope
58777.322	16.08 ± 0.01	*i*	Swope
58778.240	16.29 ± 0.01	*i*	Swope
58783.314	16.24 ± 0.01	*i*	Swope
58784.265	16.26 ± 0.01	*i*	Swope
58785.286	16.37 ± 0.01	*i*	Swope
58786.297	16.42 ± 0.01	*i*	Swope
58787.246	16.49 ± 0.01	*i*	Swope
58787.248	16.46 ± 0.01	*i*	Swope
58789.153	16.77 ± 0.01	*i*	Swope
58791.315	16.67 ± 0.01	*i*	Swope
58804.294	17.19 ± 0.01	*i*	Swope
58805.309	17.26 ± 0.01	*i*	Swope
58806.296	17.24 ± 0.02	*i*	Swope
58807.299	17.27 ± 0.01	*i*	Swope
58808.295	17.23 ± 0.02	*i*	Swope

Table A1
(Continued)

MJD	Magnitude	Filter	Telescope
58813.181	17.48 ± 0.01	*i*	Swope
58814.290	17.52 ± 0.01	*i*	Swope
58815.295	17.54 ± 0.02	*i*	Swope
58817.239	17.76 ± 0.01	*i*	Swope
58827.196	18.14 ± 0.02	*i*	Swope
58828.209	18.11 ± 0.02	*i*	Swope
58829.237	18.04 ± 0.03	*i*	Swope
58830.177	18.22 ± 0.02	*i*	Swope
58831.185	18.10 ± 0.03	*i*	Swope
58834.119	18.16 ± 0.02	*i*	Swope
58835.252	18.18 ± 0.02	*i*	Swope
58836.200	18.27 ± 0.01	*i*	Swope
58839.204	18.24 ± 0.01	*i*	Swope
58840.215	18.29 ± 0.02	*i*	Swope
58849.218	18.67 ± 0.02	*i*	Swope
58851.102	18.58 ± 0.01	*i*	Swope
58853.078	18.73 ± 0.03	*i*	Swope
58869.051	18.92 ± 0.04	*i*	Swope
58871.092	18.97 ± 0.05	*i*	Swope
58873.178	19.24 ± 0.04	*i*	Swope
58876.143	19.35 ± 0.02	*i*	Swope
58877.174	19.16 ± 0.03	*i*	Swope
58882.174	19.22 ± 0.04	*i*	Swope
58885.159	19.30 ± 0.08	*i*	Swope
58893.074	19.38 ± 0.03	*i*	Swope
58896.143	19.84 ± 0.14	*i*	Swope
58897.115	19.61 ± 0.04	*i*	Swope
58904.070	19.67 ± 0.03	*i*	Swope
58909.070	19.55 ± 0.04	*i*	Swope
58911.104	19.47 ± 0.06	*i*	Swope
58921.068	19.78 ± 0.07	*i*	Swope

Note. All the data presented in this table have been corrected for Galactic extinction. We did not perform host subtraction on the Swift UV data since the host contribution is negligible. On the other hand, the ZTF, LCO, and Swope data are all host-subtracted.

ORCID iDs

Tiara Hung https://orcid.org/0000-0002-9878-7889
Ryan J. Foley https://orcid.org/0000-0002-2445-5275
S. Veilleux https://orcid.org/0000-0002-3158-6820
S. B. Cenko https://orcid.org/0000-0003-1673-970X
Jane L. Dai https://orcid.org/0000-0002-9589-5235
Katie Auchettl https://orcid.org/0000-0002-4449-9152
Thomas G. Brink https://orcid.org/0000-0001-5955-2502
Georgios Dimitriadis https://orcid.org/0000-0001-9494-179X
Alexei V. Filippenko https://orcid.org/0000-0003-3460-0103
S. Gezari https://orcid.org/0000-0003-3703-5154
Thomas W.-S. Holoien https://orcid.org/0000-0001-9206-3460
Charles D. Kilpatrick https://orcid.org/0000-0002-5740-7747
Brenna Mockler https://orcid.org/0000-0001-6350-8168
Anthony L. Piro https://orcid.org/0000-0001-6806-0673
Enrico Ramirez-Ruiz https://orcid.org/0000-0003-2558-3102
César Rojas-Bravo https://orcid.org/0000-0002-7559-315X
Sjoert van Velzen https://orcid.org/0000-0002-3859-8074
WeiKang Zheng https://orcid.org/0000-0002-2636-6508

References

Alexander, K. D., Berger, E., Guillochon, J., Zauderer, B. A., & Williams, P. K. G. 2016, ApJL, 819, L25
Arcavi, I., Gal-Yam, A., Sullivan, M., et al. 2014, ApJ, 793, 38
Auchettl, K., Ramirez-Ruiz, E., & Guillochon, J. 2018, ApJ, 852, 37
Baldwin, J. A., Phillips, M. M., & Terlevich, R. 1981, PASP, 93, 5
Becker, A. 2015, HOTPANTS: High Order Transform of PSF ANd Template Subtraction v5.1.10, Astrophysics Source Code Library, ascl:1504.004
Bellm, E. C., Kulkarni, S. R., Graham, M. J., et al. 2019, PASP, 131, 018002
Blagorodnova, N., Cenko, S. B., Kulkarni, S. R., et al. 2019, ApJ, 873, 92
Bonnerot, C., Rossi, E. M., Lodato, G., & Price, D. J. 2016, MNRAS, 455, 2253
Breeveld, A. A., Landsman, W., Holland, S. T., et al. 2011, in AIP Conf. Ser. 1358, Gamma Ray Bursts 2010, ed. J. E. McEnery, J. L. Racusin, & N. Gehrels (College Park, MA: AIP), 373
Brown, J. S., Kochanek, C. S., Holoien, T. W.-S., et al. 2018, MNRAS, 473, 1130
Cappellari, M. 2017, MNRAS, 466, 798
Cardelli, J. A., Clayton, G. C., & Mathis, J. S. 1989, ApJ, 345, 245
Cenko, S. B., Cucchiara, A., Roth, N., et al. 2016, ApJL, 818, L32
Chornock, R., Berger, E., Gezari, S., et al. 2014, ApJ, 780, 44
Christensen, L., Fynbo, J. P. U., Prochaska, J. X., et al. 2011, ApJ, 727, 73
Clemens, J. C., Crain, J. A., & Anderson, R. 2004, Proc. SPIE, 5492, 331
Cutri, R. M., Skrutskie, M. F., van Dyk, S., et al. 2003, 2MASS All Sky Catalog of Point Sources
Dai, L., McKinney, J. C., & Miller, M. C. 2015, ApJL, 812, L39
Dai, L., McKinney, J. C., Roth, N., Ramirez-Ruiz, E., & Miller, M. C. 2018, ApJL, 859, L20
Dimitriadis, G., Rojas-Bravo, C., Kilpatrick, C. D., et al. 2019, ApJL, 870, L14
Esquej, P., Saxton, R. D., Freyberg, M. J., et al. 2007, A&A, 462, L49
Evans, C. R., & Kochanek, C. S. 1989, ApJL, 346, L13
Flewelling, H. A., Magnier, E. A., Chambers, K. C., et al. 2020, ApJS, 251, 7
Foley, R. J., Papenkova, M. S., Swift, B. J., et al. 2003, PASP, 115, 1220
Frank, J., & Rees, M. J. 1976, MNRAS, 176, 633
French, K. D., Arcavi, I., Zabludoff, A. I., et al. 2020, ApJ, 891, 93
Gallegos-Garcia, M., Law-Smith, J., & Ramirez-Ruiz, E. 2018, ApJ, 857, 109
Gatkine, P., Veilleux, S., & Cucchiara, A. 2019, ApJ, 884, 66
Gehrels, N., Chincarini, G., Giommi, P., et al. 2004, ApJ, 611, 1005
Gezari, S., Chornock, R., Rest, A., et al. 2012, Natur, 485, 217
Guillochon, J., Nicholl, M., Villar, V. A., et al. 2018, ApJS, 236, 6
Guillochon, J., & Ramirez-Ruiz, E. 2013, ApJ, 767, 25
Guillochon, J., & Ramirez-Ruiz, E. 2015, ApJ, 809, 166
Hayasaki, K., Stone, N., & Loeb, A. 2016, MNRAS, 461, 3760
Hills, J. G. 1975, Natur, 254, 295
Holoien, T. W. S., Auchettl, K., Tucker, M. A., et al. 2020, ApJ, 898, 161
Holoien, T. W.-S., Huber, M. E., Shappee, B. J., et al. 2019a, ApJ, 880, 120
Holoien, T. W.-S., Kochanek, C. S., Prieto, J. L., et al. 2016, MNRAS, 455, 2918
Holoien, T. W.-S., Prieto, J. L., Bersier, D., et al. 2014, MNRAS, 445, 3263
Holoien, T. W. S., Vallely, P. J., Auchettl, K., et al. 2019b, ApJ, 883, 111
Hung, T., Cenko, S. B., Roth, N., et al. 2019, ApJ, 879, 119
Hung, T., Foley, R. J., Ramirez-Ruiz, E., et al. 2020, ApJ, 903, 31
Hung, T., Gezari, S., Blagorodnova, N., et al. 2017, ApJ, 842, 29
Jonker, P. G., Stone, N. C., Generozov, A., van Velzen, S., & Metzger, B. 2020, ApJ, 889, 166
Kara, E., Dai, L., Reynolds, C. S., & Kallman, T. 2018, MNRAS, 474, 3593
Kochanek, C. S. 2016, MNRAS, 458, 127
Komossa, S., & Bade, N. 1999, A&A, 343, 775
Komossa, S., & Greiner, J. 1999, A&A, 349, L45
Korista, K. T., Bautista, M. A., Arav, N., et al. 2008, ApJ, 688, 108
Kurucz, R. L., & Bell, B. 1995, Atomic Line Data, CD-ROM No. 23 (Cambridge, MA: Smithsonian Astrophysical Observatory), 23
Law-Smith, J., Guillochon, J., & Ramirez-Ruiz, E. 2019, ApJL, 882, L25
Law-Smith, J., Ramirez-Ruiz, E., Ellison, S. L., & Foley, R. J. 2017, ApJ, 850, 22
Law-Smith, J. A. P., Coulter, D. A., Guillochon, J., Mockler, B., & Ramirez-Ruiz, E. 2020, ApJ, 905, 141
Leja, J., Johnson, B. D., Conroy, C., van Dokkum, P. G., & Byler, N. 2017, ApJ, 837, 170
Levan, A. J., Tanvir, N. R., Cenko, S. B., et al. 2011, Sci, 333, 199
Liu, F. K., Zhou, Z. Q., Cao, R., Ho, L. C., & Komossa, S. 2017, MNRAS, 472, L99

Lodato, G., Nayakshin, S., King, A. R., & Pringle, J. E. 2009, MNRAS, 398, 1392
Lodato, G., & Rossi, E. M. 2011, MNRAS, 410, 359
Loeb, A., & Ulmer, A. 1997, ApJ, 489, 573
Lu, W., & Bonnerot, C. 2020, MNRAS, 492, 686
Masci, F. J., Laher, R. R., Rusholme, B., et al. 2019, PASP, 131, 018003
Matsumoto, T., & Piran, T. 2021, MNRAS, 502, 3385
Metzger, B. D., & Stone, N. C. 2016, MNRAS, 461, 948
Miller, J. M., Kaastra, J. S., Miller, M. C., et al. 2015, Natur, 526, 542
Miller, J. S., & Stone, R. P. S. 1993, The Kast Double Spectrograph, Technical Report, No. 66, Lick Observatory
Miller, M. C. 2015, ApJ, 805, 83
Mockler, B., Guillochon, J., & Ramirez-Ruiz, E. 2019, ApJ, 872, 151
Mockler, B., & Ramirez-Ruiz, E. 2020, arXiv:2007.12198
Nasa High Energy Astrophysics Science Archive Research Center (Heasarc) 2014, HEAsoft: Unified Release of FTOOLS and XANADU, Astrophysics Source Code Library, ascl:1408.004
Nicholl, M., Wevers, T., Oates, S. R., et al. 2020, MNRAS, 499, 482
O'Brien, A., Kaplan, D., Murphy, T., Yu, W., & Zhang, W. 2019, ATel, 13334, 1
Oke, J. B., Cohen, J. G., Carr, M., et al. 1995, PASP, 107, 375
Oke, J. B., & Gunn, J. E. 1983, ApJ, 266, 713
Parkinson, E. J., Knigge, C., Long, K. S., et al. 2020, MNRAS, 494, 4914
Phinney, E. S. 1989, in IAU Symp. 136, The Center of the Galaxy, ed. M. Morris, 543
Piran, T., Svirski, G., Krolik, J., Cheng, R. M., & Shiokawa, H. 2015, ApJ, 806, 164
Piro, A. L., & Lu, W. 2020, ApJ, 894, 2
Planck Collaboration, Aghanim, N., Akrami, Y., et al. 2020, A&A, 641, A6
Poole, T. S., Breeveld, A. A., Page, M. J., et al. 2008, MNRAS, 383, 627
Prochaska, J. X. 2006, ApJ, 650, 272
Prochaska, J. X., Chen, H.-W., Dessauges-Zavadsky, M., & Bloom, J. S. 2007, ApJ, 666, 267
Prochaska, J. X., Dessauges-Zavadsky, M., Ramirez-Ruiz, E., & Chen, H.-W. 2008, ApJ, 685, 344
Ramirez-Ruiz, E., & Rosswog, S. 2009, ApJL, 697, L77
Rees, M. J. 1988, Natur, 333, 523
Rest, A., Scolnic, D., Foley, R. J., et al. 2014, ApJ, 795, 44
Rest, A., Stubbs, C., Becker, A. C., et al. 2005, ApJ, 634, 1103
Riess, A. G., Filippenko, A. V., Li, W., et al. 1999, AJ, 118, 2675
Roming, P. W. A., Kennedy, T. E., Mason, K. O., et al. 2005, SSRv, 120, 95
Roth, N., & Kasen, D. 2018, ApJ, 855, 54
Roth, N., Kasen, D., Guillochon, J., & Ramirez-Ruiz, E. 2016, ApJ, 827, 3
Schechter, P. L., Mateo, M., & Saha, A. 1993, PASP, 105, 1342
Schlafly, E. F., & Finkbeiner, D. P. 2011, ApJ, 737, 103
Shiokawa, H., Krolik, J. H., Cheng, R. M., Piran, T., & Noble, S. C. 2015, ApJ, 804, 85
Short, P., Nicholl, M., Lawrence, A., et al. 2020, MNRAS, 498, 4119
Siebert, M. R., Strasburger, E., Rojas-Bravo, C., & Foley, R. J. 2019, Transient Name Server Classification Report, 2019-1921, 1
Silverman, J. M., Foley, R. J., Filippenko, A. V., et al. 2012, MNRAS, 425, 1789
Strubbe, L. E., & Quataert, E. 2009, MNRAS, 400, 2070
Svirski, G., Piran, T., & Krolik, J. 2017, MNRAS, 467, 1426
Tonry, J. L., Denneau, L., Heinze, A. N., et al. 2018, PASP, 130, 064505
van Velzen, S., Anderson, G. E., Stone, N. C., et al. 2016, Sci, 351, 62
van Velzen, S., Farrar, G. R., Gezari, S., et al. 2011, ApJ, 741, 73
van Velzen, S., Gezari, S., Cenko, S. B., et al. 2019, ApJ, 872, 198
van Velzen, S., Gezari, S., Hammerstein, E., et al. 2021, ApJ, 908, 26
van Velzen, S., Holoien, T. W. S., Onori, F., Hung, T., & Arcavi, I. 2020, SSRv, 216, 124
van Velzen, S., Stone, N. C., Metzger, B. D., et al. 2019, ApJ, 878, 82
Wang, J., Xu, D., & Wei, J. 2017, FrASS, 4, 40
Weymann, R. J., Morris, S. L., Foltz, C. B., & Hewett, P. C. 1991, ApJ, 373, 23
Wu, S., Coughlin, E. R., & Nixon, C. 2018, MNRAS, 478, 3016
Xiao, T., Barth, A. J., Greene, J. E., et al. 2011, ApJ, 739, 28
Yan, L., Quimby, R., Gal-Yam, A., et al. 2017, ApJ, 840, 57
Yang, C., Wang, T., Ferland, G. J., et al. 2017, ApJ, 846, 150